
# The robust stimulation model for the EGS-reservoir in the hot magmatic environment at Acoculco and its verification against the laboratory fracking experiment

D 6.5

# The robust stimulation model for the EGS-reservoir in the hot magmatic environment at Acoculco and its verification against the laboratory fracking experiment

D 6.5

Version 1.0

Compiled by Paromita Deb, RWTH Aachen

With contribution from:
Franceso Parisio (UFZ, Leipzig),
Hannes Hofmann (GFZ Potsdam),
Peter Fokker, Eva Dekker, (TNO, Utrecht)
Stephan Dueber, Paromita Deb (RWTH Aachen)

Work package 6

08 May 2019

Website: http://www.gemex-h2020.eu

The GEMex project is supported by the European Union's Horizon 2020 programme for Research and Innovation under grant agreement No 727550

# Table of Contents

# List of figures

# List of tables

# Executive summary

*(Paromita Deb, RWTH Aachen)*

Enhanced Geothermal System (EGS) techniques are used to create permeability in hot, dry and impermeable formations by creating new fractures or by connecting existing fractures. These fractures form heat exchangers in which cold water is circulated and heated up for generating electricity at the surface.

For a successful EGS design, it is fundamental to understand the propagation of fracture under different stress conditions. Codes for designing stimulation techniques and predicting fracture growth and propagation have been used by oil industries for several decades. However, verification of these codes against real data set is generally lacking. In our study, we performed hydraulic fracturing experiments in scale which can be best controlled in the laboratory. We produced data sets, which can be used as benchmark for verification of different stimulation design tools. The experiments are well controlled in the laboratory and consists of all information, which are generally lacking when experiments are performed in the subsurface. The samples for the experiments performed within GEMex are granite and marble and are collected from Las Minas, which is considered as an exhumed system for Los Humeros and Acoculco. These samples are considered to be representative of the subsurface rocks in Los Humeros and Acoculco. The field trip was conducted with assistance of local Mexican geologist.

The experiments are performed in a true-triaxial apparatus that has been developed in the past years within a project funded by BMWi (German Federal Ministry for Economic Affairs and Energy). The details of the apparatus and experimental protocol are presented in Siebert (2017). The experiments are reported in Deliverable D 6.4 and should be referred by the reader for better understanding of the dataset used for performing the reported simulations.

Researchers from RWTH provided the experimental data set, the boundary conditions, rock and fluid parameters to the partner simulation groups in WP 6 for simulating the experiment in the laboratory. The objective was to simulate the growth and propagation of fracture as observed in the laboratory test. This report is a compilation of the work done by various simulation groups within GEMex project to simulate these hydraulic fracturing experiments. The experiments are performed in RWTH Aachen and the partner institutions involved in simulation are GFZ (Potsdam), UFZ (Leipzig) and TNO (Utrecht).

# 1 Introduction

*(Stephan Düber and Paromita Deb, RWTH Aachen)*

The hydraulic fracturing experiments for collecting dataset, which can be used as benchmark for verification of codes used for stimulation design, are performed at RWTH Aachen University. The experiment details including the set-up of the experiment, experiment protocol, input parameters and boundary conditions are reported in Deliverable D 6.4 - Report on the laboratory fracturing experiment, its boundary conditions, and its flow rates and fracture aperture versus time curves.

In this section, we briefly recall the experimental protocol and the data generated for the purpose of simulation. The main references for the theory of the experimental set up and previous work is Siebert (2017).

Within the framework of GEMex, one of the potential EGS Sites is Acoculco. It was decided to perform the hydraulic fracturing experiments using samples collected from the respective location. The lithology of the basement of Acoculco system constitutes mainly of skarns and marbles, which are formed as a result of contact metamorphism due to the granitic intrusion (Lopez-Hernandez et al., 2009). Accordingly, we decided to use representative samples of granites and skarn/marble samples to perform the hydraulic fracturing experiment. We performed experiments on two samples of granite and two samples of marble. Table 1.1.1. provides information regarding the sample locations. Petrophysical and elastic properties of the samples are reported in Deliverable D 6.4.

**Table 1.1.1: Details of sample location**

| **Type** | Skarn / Marble | Granite |
|---|---|---|
| **Location Type** | Quarry | River Bed |
| **Date** | 21.03.2017 | 21.03.2017 |
| **Location** | Pueblo Nuevo | Las Minas |
| **Country** | Mexico | Mexico |
| **State** | Veracruz | Veracruz |
| **Longitude** | 693048 | 694726 |
| **Latitude** | 2180273 | 2179109 |
| **Elevation (m a.s.l.)** | 2037 | 1260 |

## 1.1 Brief explanation on experimental protocol

The experimental procedure is presented in Figure 1.1.1. The experiment begins by applying the initial stresses ($\sigma_x$, $\sigma_y$, $\sigma_z$) on the sample, where $\sigma_x = \sigma_y$ = 15 MPa and $\sigma_z$= 5 MPa . Fluid is then pumped through the injection system to de-air the system and fill the system with injection fluid (not shown). A leakage test is done to make sure the injection system is tight. During the leakage test at ~ –1800 s, the injection system is pressurized with 3 MPa for ~ 600 s. Following this, we perform active transmission (AT) experiments on the sample under the applied initial stresses using the 32 acoustic sensors attached to the rocks through the loading plates. Every acoustic sensor is used as an emitter once while the other sensors act as receivers. The AT experiments are performed to determine an average p-wave velocity of the rock type.

After the leakage test and the AT experiments, the volume in the pump is reduced to $V_0$ = 5 cm³ and injection of fluid for hydraulic fracturing starts. The initial injection rate is 1 $cm^3$/min until a pressure of 0.5 MPa is reached and then the injection rate is reduced to 0.1 $cm^3$/min for the rest of the experiment. Simultaneously with the injection, the acoustic emission recording is activated. The starting time of the pump is used as reference time (t = 0 s) for all recorded data. The pressure rise with time versus the injection rate is monitored. Once the peak pressure is reached, a defined volume $\Delta V_p$ is further injected at the same injection rate (0.1 $cm^3$/min). This defined volume leads to controlled fracture growth within the sample dimension and has been established through series of previous experiments. After injecting the volume, $\Delta V_p$, the pump is stopped at ~ 1800 s (Figure 1.1.1). This phase of the experiment is referred to as "shut in". When the pressure in the injection system drops below the minimum confining stress ($\sigma_z$ = 5 MPa), the pressure in the injection system is released followed by the unloading of the sample.

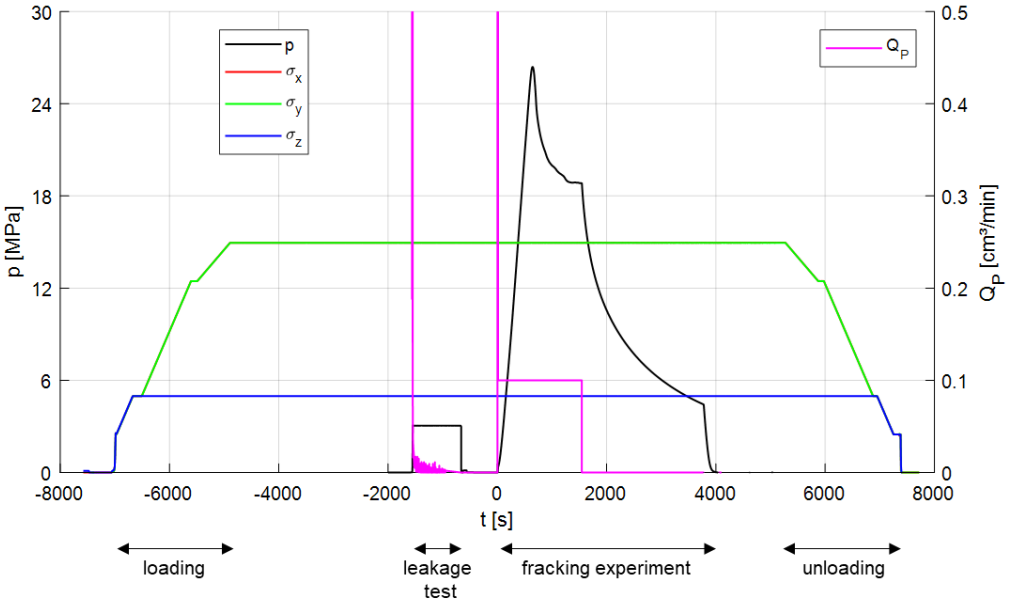


**Figure 1.1.1: Experimental procedure**

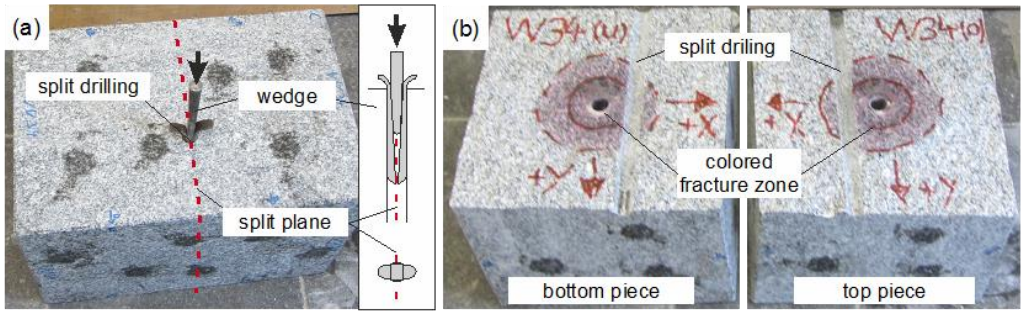


**Figure 1.1.2: Splitting the sample documentation of coloured fracture zone [2]**

When the experiment is finished, the sample is removed from the experimental setup. The packer is removed from the borehole and a second hole is drilled to split the sample. The sample is split along the fracture plane and the fluid coloured fracture zone is outlined with a marker (Figure 1.1.2). Additionally photogrammetry is used to create a 3D model of the split sample.

The main experimental data generated from these experiments include the boundary conditions of the experiment, the pressure versus injection rate curves, and the final fracture radii. The petrophysical and geomechanical properties of the rock samples and the fluid properties of the injection liquid are separately measured in the laboratory.

## 1.2 References


1. Deb et al., 2019, Report on the laboratory fracturing experiment, its boundary conditions, and its flow rates and fracture aperture versus time curves, GEMex Deliverable D 6.4
2. Lopez-Hernandez et al., 2009, Hydrothermal activity in the Tulancingo–Acoculco Caldera Complex, Central Mexico, Geothermics 38 (2009) 279-293
3. Siebert, Philipp, 2017, Laborversuche zur hydraulischen Risserzeugung in dreiaxial belasteten Granitquadern, Doctoral Dissertation, RWTH Aachen University

# 2 Numerical simulation of the Hydraulic Fracturing experiments using different simulation codes

The experiment data of the four GEMex experiments were distributed to three partner institutes involved in Task 6.3 – GFZ, TNO and UFZ with the aim of simulating the experimental data set using their respective codes.

## 2.1 Institution name: Helmholtz Centre Potsdam GFZ German Research Centre for Geosciences

*(Hannes Hofmann, GFZ Potsdam)*

### 2.1.1 Software used

Particle Flow Code 2D V4.0 (PFC2D; Itasca 2008) and FRACOD2D V5.0 (Shen 2002) were tested for their applicability to simulate the laboratory experiments described above. Both are two dimensional numerical codes with an explicit solution scheme running on single core windows PCs.

### 2.1.2 Basic Numerical model: FRACOD2D

The following description of FRACOD2D and PFC2D is taken from Hutka (2018). The FRActure propagation CODe (FRACOD) (Shen 2002) is a two-dimensional code with hydro-mechanical coupling for the numerical simulation of fracture initiation and propagation in elastic and isotropic rock media. For this purpose, FRACOD uses the Displacement Discontinuity Method (DDM) (Crouch 1976), which is based on the Boundary Element Method (BEM) (Hall 1994).

The DDM is based on the analytical solution of the following problem: let us imagine an elastic solid body in two dimension. Let the displacement field be continuous everywhere in the body except for a finite line segment where the displacements differ by a constant, the so called displacement discontinuity (Figure 2.1.1).

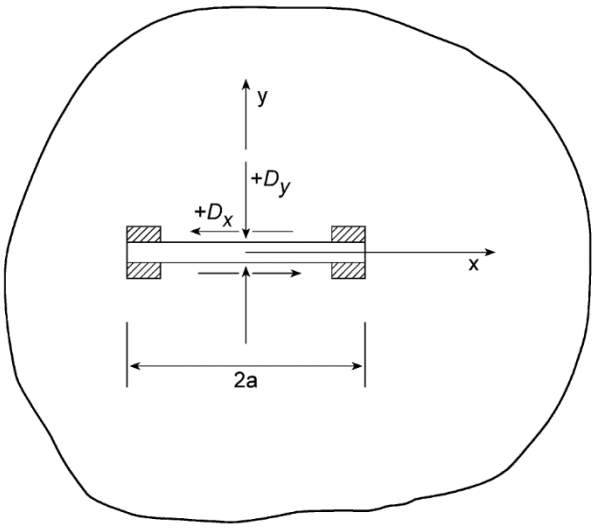


**Figure 2.1.1: Constant displacement discontinuity components $D_x$ and $D_y$ of a fracture with the length 2a in DDM (Shen et al., 2014).**

The explicit solution of this problem by Crouch and Starfield (1983) in a specific point in the body is the following:

$$\begin{aligned} \sigma_s &= A_{ss}D_s + A_{sn}D_n \\ \sigma_n &= A_{ns}D_s + A_{nn}D_n \\ u_s &= B_{ss}D_s + B_{sn}D_n \\ u_n &= B_{ns}D_s + B_{nn}D_n \end{aligned} \tag{1}$$

where $D_s$ and $D_n$ are the shear and normal components of displacement discontinuity. $A_{ss}$, $A_{sn}$, etc., and $B_{ss}$, $B_{sn}$, etc., are the boundary influence coefficients for stress and displacement, respectively. The coefficients are the functions of the elastic properties of the body and the distance from the line segment. They describe the stress and displacement field perturbed by the displacement discontinuity along the line segment.

A fracture of any shape can be modeled by N straight, sufficiently short line segments joined end to end as shown in Figure 2.1.2.

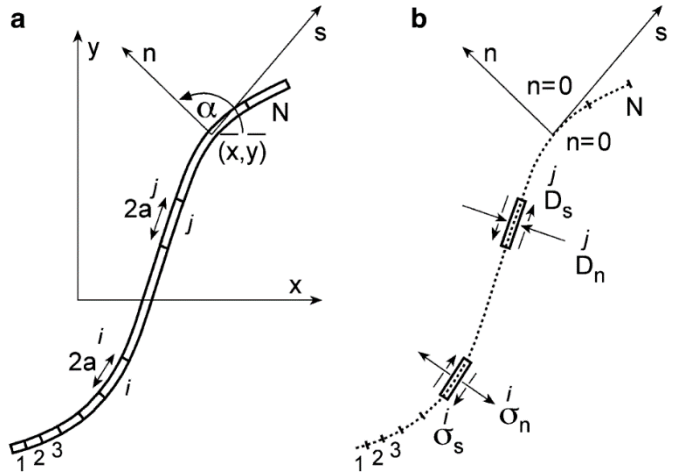


**Figure 2.1.2: Representation of a curved crack by N elemental displacement discontinuities (Shen et al., 2014).**

The displacement discontinuity can be determined for each line segment. Stresses and displacements caused by the crack at any point in the body can be calculated as the superposition of the effect of each line segments at the point of interest (Eq. 1). Applying Eq.10 to the midpoint of the $i^{th}$ line segment along the crack, the stresses and displacements can be expressed as

$$\begin{aligned} \sigma_s^i &= \sum_{j=1}^{N} A_{ss}^{ij} D_s^j + \sum_{j=1}^{N} A_{sn}^{ij} D_n^j \\ \sigma_n^i &= \sum_{j=1}^{N} A_{ns}^{ij} D_s^j + \sum_{j=1}^{N} A_{nn}^{ij} D_n^j \\ u_s^i &= \sum_{j=1}^{N} B_{ss}^{ij} D_s^j + \sum_{j=1}^{N} B_{sn}^{ij} D_n^j \\ u_n^i &= \sum_{j=1}^{N} B_{ns}^{ij} D_s^j + \sum_{j=1}^{N} B_{nn}^{ij} D_n^j \quad for\ i = 1\ to\ N \end{aligned} \tag{2}$$

If the stresses and displacements along the boundaries are given, then the unknown displacement discontinuities for the N line segments can be obtained by solving the system of equations above (Eq.

2.) using conventional numerical techniques for linear equations. For solving Eq. 2. some constraints can be added:
For an open crack, the stress components in Eq. 2. are zero, since no stresses can be transmitted through an open fracture (Eq. 3).

$$\begin{aligned} \sigma_s^i &= 0 \\ \sigma_n^i &= 0 \end{aligned} \tag{3}$$

For a closed fracture with its surfaces in elastic contact, the stress components depend on the fracture toughness $(K_s, K_n)$ and the displacement discontinuities as

$$\begin{aligned} \sigma_s^i &= K_s D_s^i \\ \sigma_n^i &= K_n D_n^i \end{aligned} \tag{4}$$

For the determination of fracture propagation FRACOD uses a mechanistic approach, the F-criterion, based on the strain-energy release rate, G. The strain energy, W, in a linear elastic body can be written as

$$W = \iiint_V \frac{1}{2}\sigma_{ij}\varepsilon_{ij}dV \tag{5}$$

where, $\sigma_{ij}$and $\varepsilon_{ij}$ are the stress and strain tensors and $V$ is the volume of the body. The strain energy can also be determined from the boundary stresses and displacements

$$W = \frac{1}{2}\int_s (\sigma_s u_s + \sigma_n u_n)ds \tag{6}$$

where $\sigma_{s,}\sigma_n$ and $u_s, u_n$ are the stresses and displacements in tangential and normal directions along the boundaries of the body, respectively.
Applying Eq. (6) to the $i^{th}$ straight line segments of a crack in an infinite body with far field stresses in the shear and normal directions of $(\sigma_s^i)_0$ and $(\sigma_n^i)_0$, the strain energy, W, in the infinite elastic body is

$$W \approx \frac{1}{2}\sum_i \left[a^i\left(\sigma_s^i - \left(\sigma_s^i\right)_0\right)D_s^i + a^i\left(\sigma_n^i - \left(\sigma_n^i\right)_0\right)D_n^i\right] \tag{7}$$

where $a^i$ is the length of the $i^{th}$ line segment, $D_s^i$ and $D_n^i$ is the shear and normal displacement discontinuity of the $i^{th}$ element of the crack respectively.
The strain energy release rate, $G$ in the direction $\theta$ at a crack tip is calculated as

$$G(\theta) = \frac{\delta W}{\delta a} \approx \frac{[W(a+\Delta a) - W(a)]}{\Delta a} \tag{8}$$

where $W(a)$ is the strain energy governed by the original crack, while $W(a + \Delta a)$ is the strain energy governed by the new crack extended by $\Delta a$ in the direction $\theta$.
To utilize the F-criterion the strain energy release rate at the fracture tip has to be divided into two parts, one due to Mode I deformation ($G_I$, pure normal displacement) and the other due to Mode II deformation ($G_{II}$, pure shear displacement). For this, a fictitious element has to be added to the fracture tip of the original crack. Then, to obtain $G_I(\theta)$ or $G_{II}(\theta)$, in Eq. (8) the shear or normal displacement has to be restricted to zero, respectively. Thereafter, the F-criterion is calculated as

$$F(\theta) = \frac{G_I(\theta)}{G_{Ic}} + \frac{G_{II}(\theta)}{G_{IIc}} \tag{9}$$

The possible direction of fracture propagation is the direction $\theta_0$ (Figure 2.1.3), for which the F-value reaches its maximum; however the fracture will propagate only if the maximum value reaches 1.0 (Shen et al., 2014).

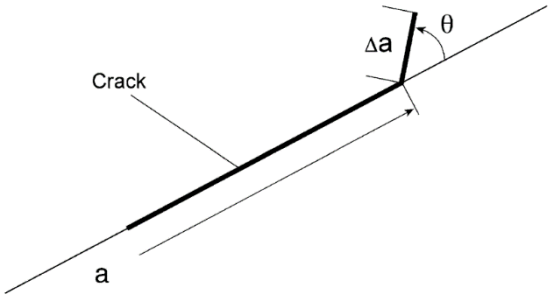


**Figure 2.1.3: Fictitious crack increment $\Delta a$ in direction $\theta$ with respect to the initial crack orientation and initial crack length, $a$ (Shen et al. 2014).**

Based on Irwin's modifications in the Griffith theory, $G_I$ and $G_{II}$ is related to the stress intensity factor $K_I$ and $K_{II}$ as

$$G_I = \frac{K_I^2}{E'}$$
$$G_{II} = \frac{K_{II}^2}{E'} \qquad (10)$$

### *Hydro-mechanical Coupling in FRACOD*

In FRACOD hydro-mechanical coupling is implemented using the explicit approach. The mechanical calculations (e.g. rock deformation, fracture propagation) are accomplished by the DDM, while the fracture fluid flow calculations are conducted through a time-marching iteration process based on the Cubic Law.

We have seen earlier, that for the mechanical calculations a finite crack was discretized into a number of DD elements. In addition to this, during the fluid flow calculations, these elements are also considered as "hydraulic domains" (Fig. 2.1.4). Two adjacent domains are connected hydraulically, so that fluid may flow from one domain into another depending on the pressure difference between them.

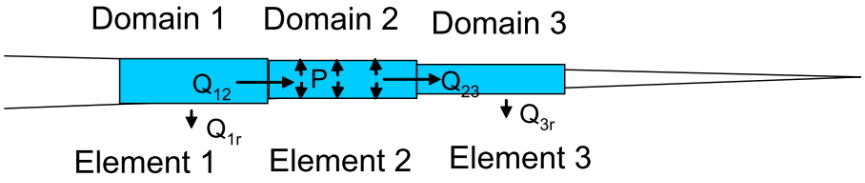


**Figure 2.1.4: Domain division for fluid flow simulation (Shen 2018).**

$\boldsymbol{Q_{ij}}$: flow rate in the fracture and leak-off into the surrounding rock; P: fluid pressure

The iteration scheme providing the solution for a coupled H – M problem in FRACOD is illustrated in Fig. 2.1.5.

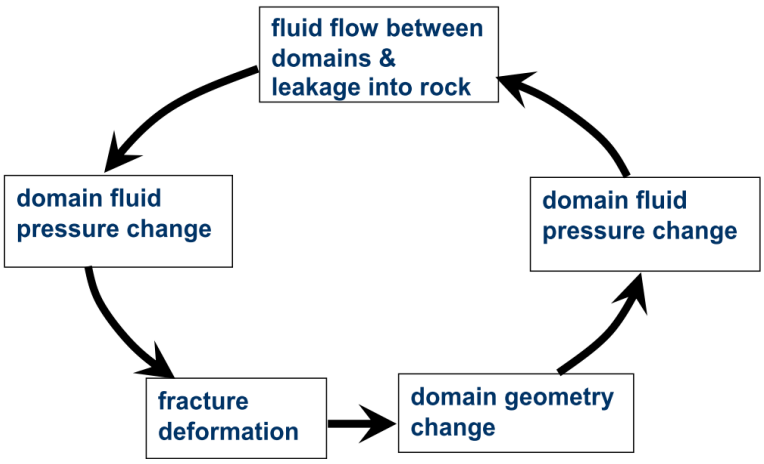


**Figure 2.1.5: Iteration scheme for a coupled hydro-mechanical process (Shen 2018).**

The iteration steps in detail are the following:

*Step 1*. Fluid flow between fracture domains and fluid leakage into the rock matrix. The flow rate, Q, between two adjacent domains is calculated by the cubic law

$$\mathrm{Q} = \frac{e^3}{12\mu}\frac{\Delta P}{l} \tag{11}$$

where $e$ is the fracture hydraulic aperture of the domain, $l$ is the element length, $\Delta P$ is fluid pressure difference between the two domains, and $\mu$ is fluid viscosity.

The fluid leak-off into the rock matrix is given as

$$\mathrm{Q_{leak}} = \frac{k_w}{\mu}\frac{P - P_0}{d} \tag{12}$$

Where $\mathrm{k_w}$is rock permeability, $P$ is the domain fluid pressure, $P_0$is the initial pore pressure, and $d$ is the effective leakage distance, which is the distance from the fracture surface where the pressure equals the initial pore pressure.

*Step 2*. The domain pressure change due to fluid flow during one time step, $\Delta t$, is calculated as

$$P(t + \Delta t) = P_0 + E_w Q\frac{\Delta t}{V} - E_w Q_{leak}\frac{\Delta t}{V} \tag{13}$$

Where $E_w$is the fluid bulk modulus and $V$ is the domain volume.

*Step 3*. The fracture deformation caused by the fluid pressure change is calculated using the DDM. For this, the new fluid pressures in fracture domains, calculated in Step 2., are the input boundary stresses. The element displacement discontinuities, influenced by the domain pressure changes, are calculated as

$$\begin{cases} \left(\sigma_s^i\right)_0 = \sum_{j=1}^{N} A_{ss}^{ij}\ D_s^i + \sum_{j=1}^{N} A_{sn}^{ij} D_s^i - K_s D_s^i \\ \left(\sigma_n^i\right)_0 + P(t+\Delta t) - P_0 = \sum_{j=1}^{N} A_{ns}^{ij}\ D_s^i + \sum_{j=1}^{N} A_{nn}^{ij} D_n^i - K_n D_n^i \end{cases} \quad (14)$$

During this step, the additional fracture deformation due to any possible fracture propagation is also considered and incorporated into the solutions.

*Step 4*. The domain volumes change again due to fracture deformation causing fluid pressure change in the domains. The domain pressures are recalculated using the equation

$$P'(t+\Delta t) = P(t+\Delta t) - E_w \frac{\Delta e \cdot l}{V} \quad (15)$$

where $\Delta e$ is the change of the fracture aperture at the element. The overwritten fluid pressures are then used to calculate the flow rate between domains in Step 1. Steps 1 to 4 are iterated until the desired fluid time is reached and a stable solution is achieved.

In order for the iteration process to converge to a stable solution, the time step should meet the following condition:

$$\Delta t < \frac{12\mu \cdot l^2}{E_w \cdot e^2} \quad (16)$$

### 2.1.3 Basic Numerical model: PFC2D

The Particle Flow Code 2D (PFC2D) (Itasca 2008) is a coupled hydro-mechanical code, based on the Distinct Element Method (DEM) and the Bonded Particle Model (BPM). The BPM, as realized in PFC2D, approaches the mechanical behavior of rocks by a set of non-uniform-sized circular or spherical rigid particles that can be bonded together at their contact points with a cement-like material, which may break. The term "particle", in this sense, has a different meaning as in the field of mechanics. In PFC, particles have a finite radius, instead of being regarded as a body of negligible size. The mechanical behavior of this system is realized by the force and moment acting at each contact, and governed by Newton's laws of motion. After Potyondy & Cundall (2004), the following assumptions are necessary to be made in the BPM:

1. The particles are circular or spherical rigid bodies with a finite mass.
2. The particles move independently of one another and can both translate and rotate.
3. The particles interact only at contacts; since the particles are circular or spherical, a contact consists of exactly two particles in 2D.
4. The particles are allowed to overlap one another, however these overlaps are small in relation to particle size, so the contact can be regarded as a point.
5. Bonds of finite stiffness can exist at contacts, and these bonds carry load and can break. The particles at a bonded contact not necessarily overlap.
6. Generalized force–displacement laws at each contact relate relative particle motion to force and moment acting on the contact.

External forces can be applied to the particle set through the movement of rigid walls along the boundaries of the assembly. These boundary forces then transfer through the particle contact bonds towards the inner particles of the assembly. The calculations performed in PFC alternate between the application of Newton's second law for determining the translational and rotational motion for each particle, and a linear force-displacement law to update the contact forces arising from the relative motion at each contact. The iteration scheme is an explicit time-stepping algorithm with constant particle velocities and accelerations for each time step (Fig. 2.1.6) (Potyondy & Cundall 2004).

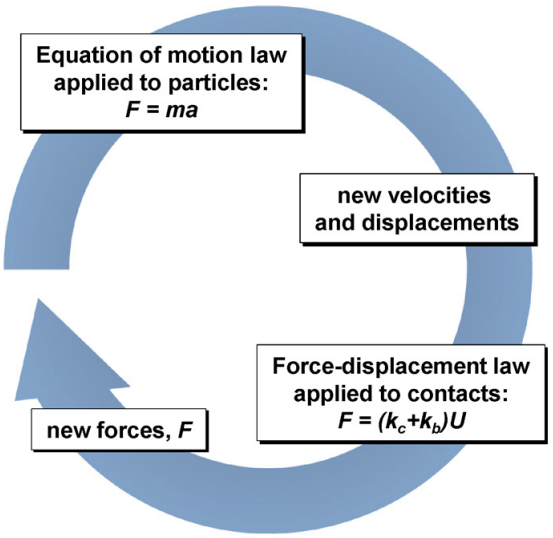


**Figure 2.1.6: Iteration scheme in PFC2D (Yoon 2014).**
m: particle mass; a: acceleration; $\boldsymbol{k_c}$: contact stiffness; $\boldsymbol{k_b}$: bond stiffness; U: particle displacement

The bonds between the particles in the BPM are so called *parallel bonds*, which correspond to a finite thickness cement material around the contact points.

The resultant force acting on a particle contact is comprised of a force, $F_i$, due particle overlap (corresponds to unconsolidated grain behavior, e.g. dry sand), and of a force and a moment, $\bar{F}_i$ and $\bar{M}_i$, carried by the parallel bond (corresponds to a finite thickness cement material around the contact points) (Fig. 2.1.7).

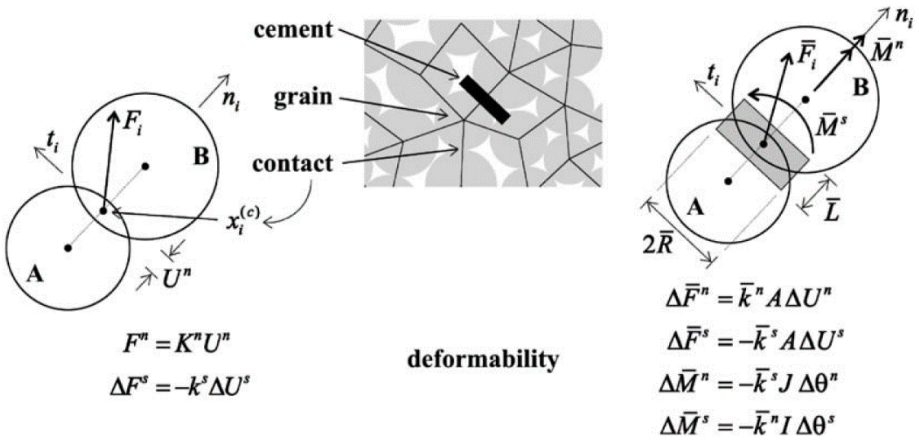


**Figure 2.1.7: Force-displacement behavior of grain-cement system (Potyondy & Cundall 2004)**

In the following, the force-displacement law will be described for these two kinds of contact behaviors.

*Particle behavior*

The following parameters are necessary to define the force-displacement law for the grains: the normal and shear stiffnesses, $k_n$ and $k_s$, and the friction coefficient between the two contacting particles, $\mu$. Whenever two particles overlap, a contact is formed at the center of the overlap region along the line joining the particle centers ($x_i^{(c)}$ in Fig. 2.1.7.). The contact stiffness (derived from the two particle stiffnesses) corresponds to two linear springs acting in series plus a slider in the shear direction.

The force, $F_i$ exerted by particle A on particle B, can be resolved into a normal and a shear component with respect to the contact plane as

$$F_i = F^n n_i + F^s t_i \tag{17}$$

where $F^n$ and $F^s$denote the normal and shear force components and $n_i$ and $t_i$ are the base vectors for the contact plane. The normal force can be calculated as

$$F^n = K^n U^n \tag{18}$$

where $U^n$ is the normal displacement and $K^n$ is the contact normal stiffness derived from the stiffnesses of the two overlapping particles.

The shear force, at the moment of the contact forming, is restricted to zero. After that during every iteration step the relative shear displacement increment, $\Delta U^s$, produces an increment of elastic shear force, $\Delta F^s$, which is (considering the rotation of the contact plane) added to $F^s$, so the increment of shear force can be given by

$$\Delta F^s = -k^s \Delta U^s \tag{19}$$

where $k^s$ is the contact shear stiffness.

The slip along the contact is defined by computing the contact friction coefficient as

$$\mu = \min(\mu^{(A)}, \mu^{(B)}) \tag{20}$$

where $\mu^{(A)}$ and $\mu^{(B)}$ are the particle friction coefficients. If $F^s > \mu F^n$ then $F^s = \mu F^n$.

*Cement behavior*

The parameters defining the parallel bond are the following: Normal and shear stiffness per unit area, $\bar{k}^n$ and $\bar{k}^s$; tensile and shear strengths, $\bar{\sigma}_c$ and $\bar{\tau}_c$; and the bond-radius multiplier, $\bar{\lambda}$, and the parallel-bond radius as

$$\bar{R} = \bar{\lambda} \min(R^{(A)}, R^{(B)}) \tag{21}$$

where $R^{(A)}$ and $R^{(B)}$ are the particle radii. Parallel bonds establish an elastic interaction between two particles and that acts in parallel with the grain-based portion of the force-displacement law. The grains can only transmit force, while the parallel bonds can transmit both force and moment.

The resultant force and moment carried by the $i^{th}$ parallel bond, $\bar{F}_i$ and $\bar{M}_i$, respectively, represent the action of the bond on particle B. After resolution to normal and shear components:

$$\begin{aligned} \bar{F}_i &= \bar{F}^n n_i + \bar{F}^s t_i \\ \bar{M}_i &= \bar{M}^n n_i + \bar{M}^s t_i \end{aligned} \tag{22}$$

With $\bar{F}^n$, $\bar{F}^s$ and $\bar{M}^n$, $\bar{M}^s$ denote the normal- and tangential directed forces and moments, respectively, while $n_i$ and $t_i$ are the base vectors of the contact plane. In 2D the in-plane moment, $\bar{M}^n$, equals to zero, while $\bar{M}^s$ acts out-of-plane. $\bar{F}_i$ and $\bar{M}_i$are calculated in an incremental manner, summing up the subsequent relative displacement- and rotation increments for each iteration step (Potyondy & Cundall 2004). The normal stress acting on a parallel bond is calculated as

$$\bar{\sigma} = -\frac{\bar{F}^n}{A} + \bar{\beta}\,\frac{|\bar{M}^s|R}{I} < \bar{\sigma}_c \tag{23}$$

where $\bar{\beta}$ is the moment-contribution factor, $A$ is the area, and $I$ is the moment of inertia as

$$\begin{aligned} A &= 2\bar{R} \\ I &= \frac{2}{3}\,\bar{R}^3 \end{aligned} \tag{24}$$

For parallel bonds the Mohr-Coulomb failure criterion applies, so Mode I (tensile) and Mode II (shear) bond breakages are also possible.

The full set of microparameters necessary for the BPM for the particles and for the bonds are the following:

particle microproperties: $E_c, \frac{k_n}{k_s}, \mu, R_{min}, D, \rho$

cement microproperties: $\bar{\lambda}, \bar{\beta}, \bar{E}_c, \frac{\bar{k}_n}{\bar{k}_s}, \bar{\sigma}_n, \bar{C}, \bar{\phi}$

where $E_c$ and $\bar{E}_c$ are Young's modulus, $\rho$ is particle density, and $\frac{k_n}{k_s}$ and $\frac{\bar{k}_n}{\bar{k}_s}$ are the normal to shear stiffness ratios for contact- and parallel bond, respectively, while $D$ is the ratio of maximum particle radius to the minimum radius, $R_{min}$ (Itasca 2012).

In order to achieve a desired set of macro-mechanical properties of the BPM, the model has to be calibrated. In PFC instead of assigning the macroproperties of the modeled rock directly to the particle assembly, the laboratory experiments–aiming to determine those properties–have to be simulated. In practice, this means, that applying a trial-and-error method, the above set of microparameters has to be changed, until the difference between the outcome of simulated and real experiments becomes reasonably small.

*Material genesis procedure*

The aim of the material genesis procedure is to create a densely packed, well connected assembly of arbitrary sized particles in equilibrium, without high locked-in forces. During the procedure the following five steps are applied:

1. *Compact initial assembly*: A material vessel of four frictionless walls is created to contain the particle assembly. In order to avoid the large particle–wall overlaps, the stiffness of the walls is larger than that of the particles. A set of randomly placed particles of a uniform size distribution ($R_i \in [R_{min}; R_{max}]$) is created. To avoid large overlaps, the initial size of each particle is only half of its final value. Then, the particle radii are increased to fill the space among them.
2. *Install specified isotropic stress:* The radii of all particles are reduced uniformly to achieve a specified isotropic stress, σ0, defined as the average of the direct stresses. These stresses are measured by dividing the average of the total force acting on opposing walls by the area of the corresponding specimen cross-section.
3. *Reduce the number of „floating" particles:* An assembly of non-uniform-sized circular particles that are placed randomly and compacted mechanically can contain a large number of "floating" particles that have less than three contacts. Such particles are removed in order to create a highly interlocked collection of grains.
4. *Install parallel bonds:* The parallel-bond properties are assigned to all particles that are closer to each other than $10^{-6}$ times the mean particle radius. The parallel bond properties are assigned (with a Gauss distribution) to satisfy the constituting equations.
5. *Remove from material vessel:* In the last step of the procedure the specimen is removed from the material vessel and the assembly is allowed to relax. It is done by deleting the vessel walls and iterating until static equilibrium is achieved. These internal forces under equilibrium correspond to locked-in stresses, which exist in real rock specimen (Potyondy & Cundall 2004).

*Hydro-mechanical coupling in PFC2D*

With the fluid flow algorithm, described by Yoon et al. (2014), a hydraulic treatment can be simulated in a BPM. For the fluid flow simulation each particle contact is treated as a flow channel with a hydraulic aperture, $e$. These channels connect pore spaces enclosed by neighboring particles (Fig. 2.1.8).

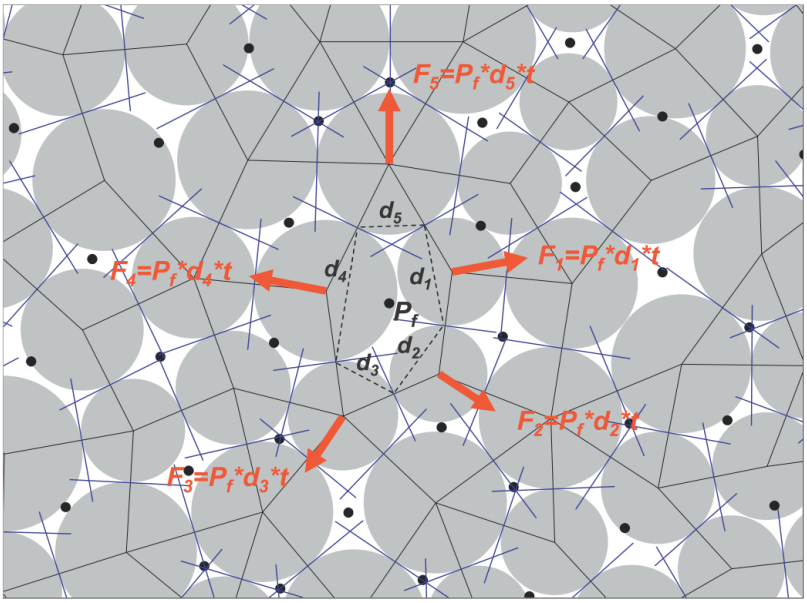


**Figure 2.1.8: Pore network model. Flow channels (blue lines at the particle contacts) are connecting two neighbouring pore spaces bound by polygons. Black dots at the polygon centers are virtual pores where pressure ($P_f$ ) is stored. Red arrows are resultant forces applied to the particles surrounding the pore space due to the pore fluid pressure (Yoon 2014)**

Pressure can be stored in the pores and (same as in FRACOD) the flow is governed by the cubic law:

$$Q = \frac{e^3 \Delta P_f}{12 \mu L} \tag{25}$$

where L is the channel length, $\Delta P_f$ is the pressure difference between the pores and $\mu$ is fluid dynamic viscosity.

The hydraulic aperture, $e$, of the flow channels is a function of effective normal stress, $\sigma_n$, at the particle contact as follows

$$e = e_{inf} + (e_0 - e_{inf}) \exp(-\alpha \sigma_n) \tag{26}$$

where $e_{inf}$is the hydraulic aperture at infinite normal stress, while $e_0$ is hydraulic aperture at zero normal stress. $\alpha$ is a constant that dictates the slope of the curve.

The pressure increase, $\Delta P_f^i$, in the $i^{th}$domain can be calculated as:

$$\Delta P_f^i = \frac{K_f}{V_d^i} (\sum Q^i \Delta t - \Delta V_d^i) \tag{27}$$

where $K_f$is fluid bulk modulus, $\Delta t$ is the time step, $V_d^i$ is the volume-, $\sum Q^i$ is the sum of inflow and outflow-, and $\Delta V_d^i$ is the volume change of the $i^{th}$ domain (Yoon et al. 2014).

The iteration scheme for the coupled hydro-mechanical simulation in PFC is similar as it was described for FRACOD, with the important difference, that during the calculations, in PFC, the broken bonds are assigned with a constant hydraulic aperture of $e_0$, while in FRACOD, the flow channel aperture is always a function of normal displacement.

### 2.1.4 Numerical model vs analytical solution

No comparison between numerical results and analytical solution is shown here. Reasons are explained in the discussion section. Modelling results from PFC2D and FRACOD2D with adapted parameters and sensitivity analysis are provided by Hutka (2018) for a similar experiment.

### 2.1.5 Numerical model vs experimental data set

No comparison between numerical results and experimental data is shown here. Reasons are explained in the discussion section. Modelling results from PFC2D and FRACOD2D with adapted parameters and sensitivity analysis are provided by Hutka (2018) for a similar experiment.

### 2.1.6 Discussion

The time step size required for a convergent numerical solution $\Delta t$ in FRACOD2D can be calculated using Equation 16. It can be seen that a low viscosity $\mu$, a high bulk modulus $E_w$, a small element size l, and a large aperture, e all lead to a decrease in time step and thus calculation time.

Reasonable calculation times can only be achieved with time step sizes in the order of 1e-4 seconds or larger. In the laboratory experiment a fluid with viscosity of 0.55 Pas and bulk modulus of 4e9 Pa was used. These parameters are fixed. Element size and fracture aperture maybe changed within a reasonable range. The element size is partly restricted by numerical stability and partly by the dimension of the initial notch. The notch has a rad–ius of 7e-3 m starting from the borehole wall. Therefore, geometrically, the smallest element length is 7e-3 m. For stable results this number should be reduced (e.g., 7e-4 m). The aperture of pressurized tensile fractures is at least in the order of 10e-6 m. Larger pressures in the fracture lead to larger apertures. A more reasonable lower estimate of a fluid-filled fracture aperture is 100e-6 m (e.g., Hofmann et al., 2016). For the time step size calculation, the maximum aperture has to be used to ensure numerical stability.

Table 2.1.1 shows the resulting time step size for different parameter combinations. It is striking that no converging solution can be achieved within a reasonable time when simulating the laboratory experiments. However, at field scale, a fast and converging solution can be achieved. This is mainly due to the significantly larger model dimension, and thus element size.

**Table 2.1.1: Comparison of the time step size for input parameters in FRACOD2D at laboratory scale and at field scale. While the converging solution for the laboratory experiment is not fast enough, simulation time is fast for field scale applications.**

| Scale | $\mu$ (Pas) | $E_w$ (Pa) | l (m) | e (m) | $\Delta t$ (s) | Fast? | Converging? |
|---|---|---|---|---|---|---|---|
| Lab | 0.55 | 4e9 | 7e-4 | 100e-6 | 8.1e-8 | No | Yes |
| Lab alt 1 | 0.55 | 4e9 | 7e-3 | 100e-6 | 8.1e-6 | No | No |
| Lab alt 2 | 0.55 | 4e9 | 7e-4 | 10e-6 | 8.1e-6 | No | No |
| Lab alt 3 | 0.55 | 4e9 | 7e-3 | 10e-6 | 8.1e-4 | Yes | No |
| Field | 1e-3 | 2e9 | 5 | 100e-6 | 1.5e-2 | Yes | Yes |

Due to the unreasonable calculation times it is recommended to test the software with a radial symmetric model around the wellbore. Alternatively, the simulation speed may be increased

significantly by parallel computing. This is currently implemented in the 3D version of the code (FRACOD3D). In the future, FRACOD2D/3D may thus be able to model this specific laboratory experiment.

Similar to FRACOD2D, the time step becomes too small for converging numerical solutions in PFC2D when using the given parameters of the experiment. Again, improving of the efficiency of the code and parallel computing may result in the required time step size reduction to model this experiment in three dimensions.

### 2.1.7 Conclusion

While the hydraulic rock fracturing process in homogeneous (FRACOD) and heterogeneous (PFC) materials intersected by discontinuities can in principle be modelled with the tested codes, it is currently not possible to model the provided laboratory experiments with either FRACOD2D V5.0 or PFC2D V4.0. This is because the required time step size for a stable numerical solution is too small when the real fluid properties, realistic fracture apertures and small enough element sizes are used. Therefore, these codes could not be verified by the provided laboratory experiments. For field scale applications this problem becomes less pronounced due to the larger element size. Necessary code development and parallelization efforts are ongoing for FRACOD3D and PFC3D in order to overcome this limitation.

### 2.1.8 References


1. Crouch, S. L., 1976, Solution of plane elasticity problems by the displacement discontinuity method. I. Infinite body solution, International Journal for Numerical Methods in Engineering, 10(2), 301-343.
2. Crouch, S. L., Starfield, A. M., Rizzo, F. J., 1983, Boundary element methods in solid mechanics, Journal of Applied Mechanics, 50, 704.
3. Hall, W. S., 1994, Boundary element method. In The Boundary Element Method, Springer, Dordrecht, 61-83.
4. Hofmann, H., Blöcher, G., Milsch, H., Babadagli, T., & Zimmermann, G., 2016, Transmissivity of aligned and displaced tensile fractures in granitic rocks during cyclic loading. International Journal of Rock Mechanics and Mining Sciences, 87, 69-84.
5. Hutka, Gergö, 2018, Benchmark modelling of true-triaxial laboratory hydraulic fracturing experiments, Master Thesis, Eötvös Loránd University, Budapest
6. Itasca Consulting Group Inc., 2008, PFC2D 4.0 (Particle Flow Code in 2 dimensions), Minneapolis, USA, Itasca Consulting Group Inc.
7. Itasca Consulting Group Inc., 2012, Technical Memorandum - 5.0 Parallel Bond Enhancement.
8. Shen, B., 2002, FRACOD Version 1.1 user's manual, FRACOM Ltd., Kyrkslätt, Finland.
9. Shen, B., Stephansson, O., & Rinne, M., 2014, Modelling rock fracturing processes, Springer Netherlands.
10. Shen, B., 2018, Modeling Rock Fracturing Processes with FRACOD, Hydraulic Fracture Modeling, 265-321.
11. Siebert, Philipp, 2017, Laborversuche zur hydraulischen Risserzeugung in dreiaxial belasteten Granitquadern, Doctoral Dissertation, RWTH Aachen University
12. Potyondy, D. O., Cundall, P. A., 2004, A bonded-particle model for rock. International journal of rock mechanics and mining sciences, 41(8), 1329-1364.
13. Yoon, J. S., Zang, A., Stephansson, O., 2014, Numerical investigation on optimized stimulation of intact and naturally fractured deep geothermal reservoirs using hydro-mechanical coupled discrete particles joints model, Geothermics, 52, 165-184.

## *2.2* Institution name: TNO

*(Peter Fokker, Eva Dekker, TNO Utrecht )*

### 2.2.1 Introduction

In the hydrocarbon industry, various numerical models have been developed to simulate hydraulic fracturing. One of these is MFrac™. MFrac™ is a pseudo-3-D modelling tool build to simulate in-field fracturing. It is unknown if this tool can be used to simulate small-scale petrophysical experiments on EGS reservoir rock. This is the knowledge gap that this research aims to close. Closing this knowledge gap would not only serve the GEMex project. If it can be shown that MFrac™ can accurately simulate laboratory petrophysical experiments, it gains an additional function as a tool for the greater scientific community.

### 2.2.2 Theoretical Background

The response of a rock to stress depends on various factors, including the level of stress, the amount of accumulated strain, the temperature, the confining pressure, and the amount of pore fluid present [Fossen, 2010]. Fracture mechanics concern the response of rocks to stress in the brittle regime, where the material fractures soon after the elastic limit has passed [Young & Friedman, 2012].

In the brittle regime a rock will accumulate elastic strain and deform until a critical stress is reached, at which point the rock fractures [Fossen, 2010]. There are three modes of fracturing: Mode I (tensile fracture, opening/extension), Mode II (shear fracture, sliding), and Mode III (shear fracture, tearing) [Fossen, 2010].

Mode I fractures form in the tensile or extensional regime, where the confining pressure is negative. These fractures open perpendicular to $\sigma_3$. The Griffith fracture criterion describes fracturing in the tensile regime:

$$\sigma_s^2 + 4T\sigma_n = 4T^2 = 0$$

Where $\sigma_s$ is the critical shear stress, T is the tensile strength of the rock, and $\sigma_n$ is the normal stress acting on the point of potential fracture.

Mode II and III fractures are shear fractures, which form in the compressional regime (positive confining pressure). Here, the critical stress needed to fracture a rock depends on the normal stress across the potential shear plane. The normal stress increases with the confining pressure of a rock, and with a larger normal stress a greater amount of shear stress is needed to fracture the rock. This relationship is described by the Mohr-Coulomb failure criterion:

$$\sigma_s = C + \sigma_n \tan\phi$$

which is also expressed as

$$\tau = S_0 + \sigma_n \mu$$

Where $\tau$ is the critical shear stress, C or $S_0$ is the internal strength or the cohesion of a rock, and $\tan\phi$ or $\mu$ is the coefficient of internal friction. The internal strength of a rock is twice the tensile strength: C = 2T.

Figure 2.2.1 shows a Mohr diagram in which the Griffith, Coulomb, and Von Mises failure criteria are plotted, creating a failure envelope. The Von Mises criterion applies to deformation in the ductile regime.

A Mohr circle below the failure envelope represents a stable state of stress. A Mohr circle touching or crossing the failure criterion represents a critical or unstable state of stress, respectively. In this state of stress, a fracture will form.

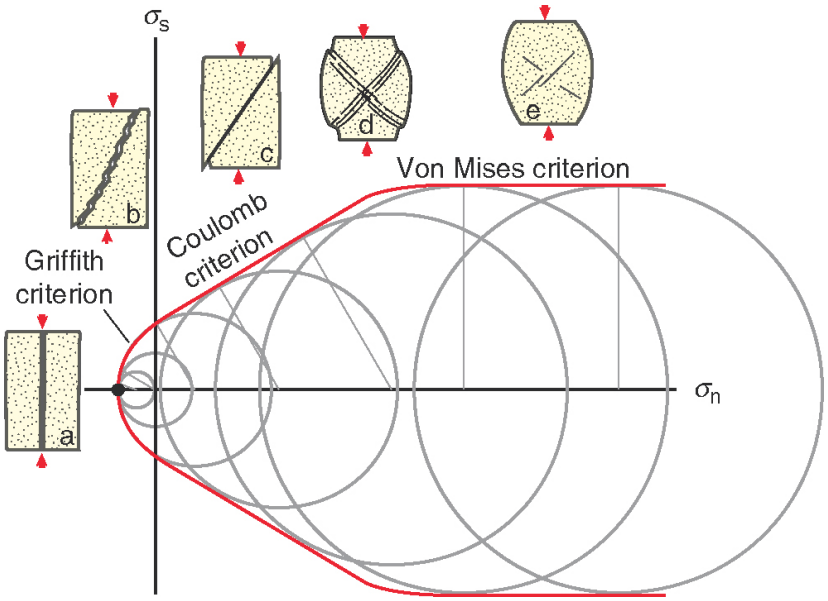


**Figure 2.2.1: The fracture criteria shown in Mohr space. The mode of fracturing is related to the confining pressure. The Griffith criterion applies to the tensile regime (negative confining pressure, Mode I fractures), while the Coulomb criterion applies to the compressional regime (positive confining pressure, Mode II and III fractures). Figure taken from H. Fossen (2010).**

The line crack problem deals with the physics of Mode I fracture propagation and growth. It is a state of stress "snapshot" of a propagating fracture, during which it is considered to be momentarily in equilibrium [Valkó and Economides, 1995]. By treating it as such, the principles of linear elasticity may be applied.

In constant pressure, the crack is treated as a line while having an elliptical shape. Valkó and Economides [1995] argue that this approach is justifiable when the width of the fracture is orders of magnitude smaller than its length, as is the case with hydraulically induced fractures.

The solution to the line crack problem makes it possible to simulate the growth of fractures as (pseudo) 3-D numerical models.

### 2.2.3 Numerical model vs analytical solution

Physics models are mathematical representations of reality. A model is created by solving partial differential equations using continuum mechanics, which means that the materials are treated as a continuous medium rather than individual particles (e.g. atoms or molecules) [Gerya, 2010, Ismail-Zadeh & Tackley, 2010]. A numerical model involves solving the partial differential equations for small, discrete time steps and on a discrete analog of space, thus simulating the evolution of a medium in space over time. The strength of numerical models is that they can deepen both quantitative and qualitative understanding of geophysical processes.

Literature defines three classic hydraulic fracturing models: the Perkins-Kern-Nordgren (PKN) model, the Kristianovitch-Geertsma-de Klerk (KDG) model, and the penny-shaped model [Perkins & Kern, 1961, Nordgren, 1972, Geertsma & De Klerk, 1969, Geertsma & Haafkens, 1979, Meyer, 1986, Valkó & Economides, 1995]. The PKN and KDG models are two-dimensional, the penny-shaped model is 2-D cylindrical. Between the two 2-D models, the PKN is used to model fractures that have a much greater length than height, while the KDG is used when the fracture height is greater than its length [Geertsma & Haafkens, 1979, Valkó and Economides, 1995]. For further information, the reader is referred to Valkó and Economides [1995]. We only make use of the penny-shaped model and as such will lay our focus there.

As the name suggests, the penny-shaped model simulates a radial fracture with a constant radius R. The cross-cut shape of the fracture is elliptical.

There are many penny-shaped fracture designs. Our models are built in MFrac™, which makes use of the penny-shaped model as designed by Meyer (1986).

We also used Dontsov's approximate analytic solution for a penny-shaped hydraulic fracture to analyze the laboratory hydraulic fracturing experiments performed in RWTH Aachen and the MFrac™ models [Dontsov, 2016]. Dontsov developed an approximate solution for a penny-shaped model whose fracture geometry is governed by three competing processes associated with the fracture toughness, viscosity, and leak-off. He proves that the fracture propagation of such a model has four limiting regimes of propagation. These regimes are also named the four vertex solutions. The four regimes as defined by Dontsov are: the storage viscosity (M vertex), leak-off viscosity (M' vertex), storage toughness (K vertex) and leak-off toughness (K' vertex). Each regime is defined by two processes in which one of two conflicting mechanisms dominates: either a viscosity- or rock toughness-associated dissipative mechanism, and either fluid storage in the fracture or fluid leak-off into the surrounding rock. Each vertex limit of the solution has a regime-specific pressure-time relationship. As such, Dontsov's solution can be used to analyze the P(t) curve of a hydraulic fracturing experiment or model to evaluate if fracture propagation was viscosity- or toughness-dominated. The P(t) relationships of the M, M', K, and K' vertices are shown as

$$P(0,t) \propto t^{-\frac{1}{3}} \quad (M)$$
$$P(0,t) \propto t^{-\frac{3}{16}} \quad (M')$$
$$P(0,t) \propto t^{-\frac{1}{5}} \quad (K)$$
$$P(0,t) \propto t^{-\frac{1}{8}} \quad (K')$$

MFrac™ is a fracture design and evaluation simulator and part of the Meyer suite of hydraulic fracture design and analysis software [Meyer, 2011]. The software and the user interface design are built towards the hydrocarbon industry, and the suite is marketed as a well stimulation design tool for both conventional and unconventional plays [Baker Hughes].

MFrac™ is built to allow both fracture design and well treatment analysis. It has options for both 2-D and 3-D (penny-shaped) fracture geometry. However, the penny-shaped model is not fully 3-D: it falls between a pseudo-3-D and fully 3-D model [Meyer, 2011]. Another limitation of the program is that fractures are initiated in a perfect unfractured medium, which of course is not the case in the field or laboratory.

The governing equations of MFrac™ are as follows [Meyer, 2011].

1. Mass conservation
2. Mass continuity equation
3. Momentum conservation
4. Width-opening pressure elasticity condition
5. Fracture propagation criteria

Additionally, the model has parametric relationships that differ between viscous dominated or toughness dominated fracture propagation. These relationships affect fracture characteristics and pressure response [Meyer, 2011].

### 2.2.4 Models vs experimental data set

The goal of this research is to find out if it is possible to simulate hydraulic fracturing laboratory experiments with the MFrac™ hydraulic fracturing software. The challenge is the fact that laboratory experiments work on isolated samples and create fractures with a radius on the scale of centimeters, while MFrac™ was built for in-field simulations, with fractures on a scale of meters. This makes scaling necessary.

The research question was thus as follows:

To what extent can modelling and simulation software MFrac™, which was developed for hydrocarbon exploration, be applied to simulate hydraulic fracturing laboratory experiments, and what can be learned from using this model to simulate such experiments?

For a detailed description of the sub-questions originating from the research and the research steps followed to answer those we refer to the report by Dekker [2018]. Here we limit ourselves to the main subjects and the key outcomes.

**Scaling**

To test and compare the results of scaling, every set of models has a reference model. Scaling is performed in such a way that the width / length ratio of created fractures is maintained. Based on the scaling methods and assumptions, the following model properties are scaled for all models: the fracture stratum height, the area of the perforation zone, and the injection flow rate. When scaling the reference injection rate $q_0$ with a factor $S$, other reference parameters (reference length $L_0$, reference width $w_0$, reference performation area $A_{perf,0}$, toughness $K_{Ic,0}$) are also scaled to new values:

$$L = L_0 S^{\frac{1}{3}}$$

$$w = w_0 S^{\frac{1}{3}}$$

$$A_{perf} = A_{perf,0} S^2$$

For some models the fracture toughness $K_{Ic}$ is scaled to the n$^{th}$ degree:

$$K_{Ic} = K_{Ic,0} S^{\frac{1}{n}}$$

For a toughness-dominated we expect *n* to be 6 [Dekker, 2018].

**MFrac™ Model Family 1**

In the first Model Family we benchmarked MFrac™ by testing how models can be most accurately linearly scaled. In 10 Model Sets we investigate the influence of the perforation area on the fracture growth, and the effect of scaling either q or $K_{IC}$.

The results of Model Set 1 show that beyond a certain minimum, the size of the perforation area doesn't influence the fracture growth.

The scaling of the injection rate, which was tested in Model Set 2 and 3, showed that the length-to-width ratio increases as S increases. This is in line with natural fracture propagation mechanisms, where a fracture's length increases at a greater rate than its width. However, the difference in injection flow-rate scaling results in a difference in accuracy. Scaling q by $S^3$ (Set 2) resulted in an accuracy over twice as low compared to scaling q linearly with S (Set 3). Therefore we chose to use the second scaling relationship for the rest of the research.

Model Sets 4 through 8 investigated the effect of scaling $K_{IC}$ to different degrees $\left(\frac{1}{2}, \frac{1}{3}, \frac{1}{4}, \frac{1}{5}, \frac{1}{6}\right)$. Model Set 4 shows a strong reversal of the increase in length-to-width ratio observed in Model Sets 2 and 3. Instead the width strongly relatively increased with scaling, while the length relatively decreases. This trend weakened as $K_{IC}$ was scaled up to a lesser degree. Model Set 8 scales $K_{IC}$ by $S^{\frac{1}{6}}$. The result is a perfectly scaled model. This shows that it is possible to linearly scale fractures in MFrac™, and that the method to do so is in line with the relationship. Model Sets 9 and 10 repeated the experiments of Model Set 3 and 8 using a more viscous fluid. The resulting accuracies are on the same level as the low viscosity model runs. Thus it can be concluded that using glycerol as the injection fluid doesn't affect the results within the MFrac™ framework. Furthermore, model 10F shows that the models can be scaled accurately even for a high scaling factor S.

Based on the Model Family 1 results, it can be concluded that it is possible to accurately scale models in MFrac™, and that the scaling isn't affected by the high viscosity of glycerol.

**MFrac™ Model Family 2**

Model Family 2 consists of two sets of scaling models that mimic Aachen experiment VV32. This means that experiment VV32 itself is the reference model. The thickness of the cap and bottom strata is set at 500 m, while fracture stratum is scaled after the Aachen specimen block. The model treatment schedule follows the second injection cycle of experiment VV32. The injection flow rate q is scaled by S. The fracture toughness is scaled by $K_{Ic} = K_{Ic,0} S^{\frac{1}{6}}$. For the first model set, a fracture was only created for the largest scaling factor. This means that fracture initiation is not controlled by the injected volume. The simulator needs either a minimum injection rate q or a minimum BHTP before a fracture is created.

This largest scaling factor was used for the second model set; and it varied the reference fracture toughness value. The results showed that changing the reference fracture toughness to the lower and upper uncertainty boundaries had a significant effect on the accuracy: a shift of 3.5%. Considering that the measured Young's Modulus and Poisson's ratio of Granite VV32 also come with uncertainties, the accuracy of model 11G can be considered within the margin of natural variation.

The results of Model Family 2 show that the fracture results of experiment VV32 can be repeated quite accurately in the simulator, but that there is a minimum scaling factor S below which no fracture

will form. We took this result into account for Model Family 3 by only using a scaling factor of 250 and 300.

**Table 2.2.1: Comparison of model results to experiment VV32**

| Experiment / Model | VV 32 | 11G | 12A | 12B |
|---|---|---|---|---|
| Scaling factor | - | 300 | 300 | 300 |
| Toughness [MPa $m^{1/2}$] | 1.6 | 1.6 | 1.3 | 1.9 |
| Fracture radius [m] (deviation) | 0.068 | 0.077 (+12.9%) | 0.079 (+16.4%) | 0.074 (+9.4%) |

## MFrac™ Model Family 3

Model Family 3 consists of eight sets of scaling models that mimic the RWTH HF experiments Marble 01 (GEMex 04), Marble 02 (GEMex 06), and Granite 02 (GEMex 07). The thickness of the strata is set up the same as for Model Family 2. The model treatment schedules are the same as the experiment treatment schedules. The injection rate is scaled by a factor S; the fracture toughness by $K_{Ic} = K_{Ic,0} S^{\frac{1}{6}}$.

The general results of Model Family 3 are in line with the findings of Model Family 2. The accuracies of the models for Marble 01 and Granite 02 are comparable to those of the model for VV32, in the order of 10-20% mismatch. Changing the reference fracture toughness to the lower or upper boundary results in a comparable shift in accuracy. It is noteworthy that the accuracies for these models are improved by using the lower $K_{IC}$ boundary, while the accuracy of the model for VV32 is improved by using the upper boundary.

**Table 2.2.2: Comparison of model results to experiment Marble 01**

| Experiment / Model | Marble 01 | 13B | 14A | 14B |
|---|---|---|---|---|
| Scaling factor | - | 300 | 300 | 300 |
| Toughness [MPa $m^{1/2}$] | 1.15 | 1.15 | 0.63 | 1.67 |
| Fracture radius [m] (deviation) | 0.0678 | 0.0569 (-14.6%) | 0.0613 (-9.6%) | 0.0544 (-20%) |

**Table 2.2.3: Comparison of model results to experiment Granite 02**

| Experiment / Model | Granite 02 | 19B | 20A | 20B |
|---|---|---|---|---|
| Scaling factor | - | 300 | 300 | 300 |
| Toughness [MPa $m^{1/2}$] | 2.39 | 2.39 | 2.36 | 2.42 |
| Fracture radius [m] (deviation) | 0.101 | 0.0833 (-17.5%) | 0.0836 (-17.2%) | 0.0831 (-17.7%) |

For the Marble 2 experiments, the accuracies are much lower than those of the scaled Marble 01, Granite 02, and VV32 models. They are in the order of 50 – 100%.

Model Family 3 confirms the conclusions made based on Model Family 2. MFrac™ can be used to accurately simulate the radius of the fractures, though only starting at a certain scaling factor that lies between 250 and 300. For a detailed discussion we again refer to Dekker's report [2018].

## P(t) analysis

We also employed Dontsov's approximation of a penny-shaped model. The four distinct pressure-time relationships were applied to the treatment schedule of the Aachen experiments from the moment of

peak pressure until the end of fluid injection. The best-fitting curves were determined through the method of least squares. Additionally, the same analysis was applied to the three models that correspond to the Aachen experiments. The goal of these analyses was to see if the fracture propagation was dominated by processes related to the viscosity or the fracture toughness.

Figure 2.2.2 (left) shows the P(t) analysis of experiment Marble 01. The K' vertex is a nearly perfect fit. The corresponding model 13B (Figure 2.2.2 - right) also has the K' vertex as the best overall fit, though vertices M' and K fit better at the start of pressure drop. This result is surprising: the limiting regime of the K' vertex is leak-off toughness, yet as a boundary condition both the experiment and the model don't experience leak-off.

Figure 2.2.3 (left) shows the P(t) analysis of experiment Marble 02. There is not one vertex curve that is a clear best fit. This means that there was not one regime that dominated the fracturing process. The corresponding model 15B (Figure 2.2.3 - right) also doesn't have one best fit: the M' and K vertices both follow the P(t) curve quite well. These vertices represent opposite regimes: leak-off viscosity and the storage toughness, respectively. This is an ambiguous result.

Figure 2.2.4 (left) shows the P(t) analysis of experiment Granite 02. None of the vertices fit the P(t) curve of the experiment: there isn't a dominant regime. This is not the case for Model 19B (Figure 2.2.4 - right). For this model, just like model 13B, the K' vertex is a good fit.

The P(t) analysis of model 13B and 19B has a clear result: the K' vertex is the best fit. The K' vertex is the limiting regime of leak-off and toughness. That the fracture propagation is dominated by toughness and not by viscosity is not surprising, given the fact that the models are scaled by scaling the fracture toughness $K_{IC}$. But that the leak-off regime dominates over the process of fluid storage in the fracture is surprising, given the fact that models are programmed to not experience leak-off. Model 15B however does not have one clear dominant regime. The M' and K vertices both are a reasonable fit of the simulated P(t) curve. These two vertices are linked to opposite regimes, making this an ambiguous result.

The P(t) analysis results of the experiments are also less evident. Only Marble 01 has a clear result. For this experiment, the K' vertex is again the dominant regime. The overlap in result between Marble 01 and model 13B validates the result of the simulation. Additionally, it affirms that the fracturing process of experiment Marble 01 was not affected by the choice of a highly viscous fracture fluid. However, the analyses of Marble 02 and Granite 02 does not show a clear dominant regime. For Marble 02, both the M' and K vertices approximate the P(t)-curve. For Granite 02, there is no clear dominant vertex whatsoever. This indicates that it is likely that these two fracturing experiments were the result of both toughness- and viscosity-related processes. We recommend caution when applying these results to field simulations and design. Because the fracture propagation has been affected by the high viscosity of the glycerol, these results do not linearly translate to the field where much less viscous fluids are used to fracture.

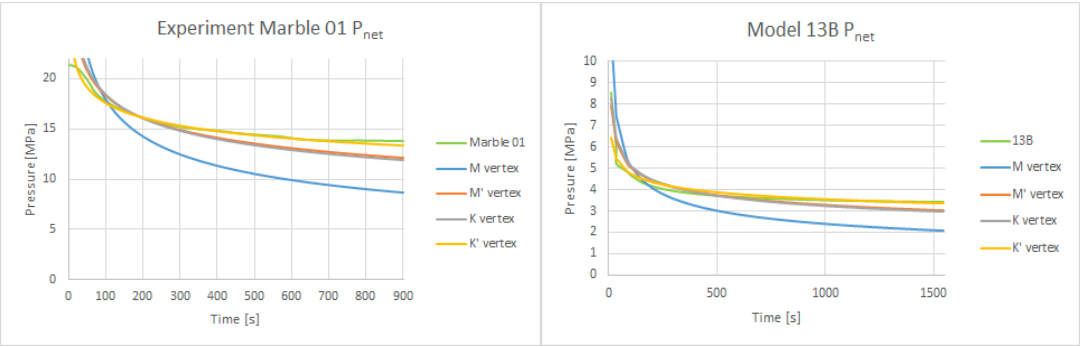


**Figure 2.2.2: P(t) curve of the Marble 01 experiment (left) and the corresponding model 13B (right), until the end of pumping. The K' vertex is a nearly perfect fit**

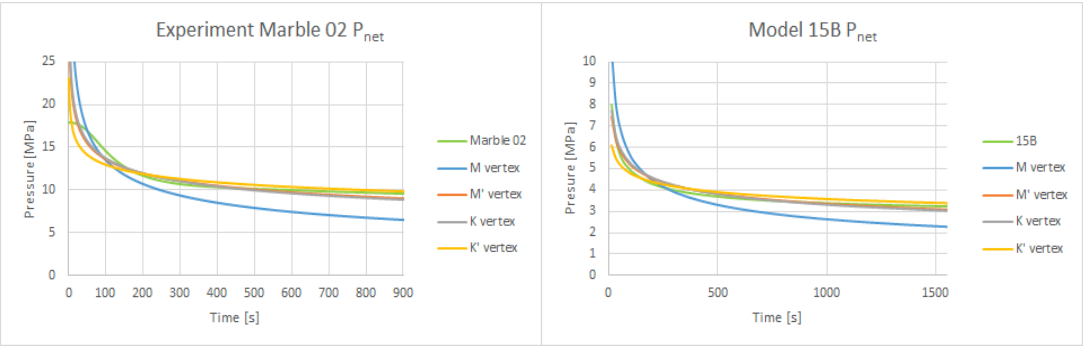


**Figure 2.2.3: P(t) curve of the Marble 02 experiment (left) and the corresponding model 15B (right), until the end of pumping. No good fit for the experiment is obtained due to startup of the experiment. For the model both K and M' vertex fit reasonably well.**

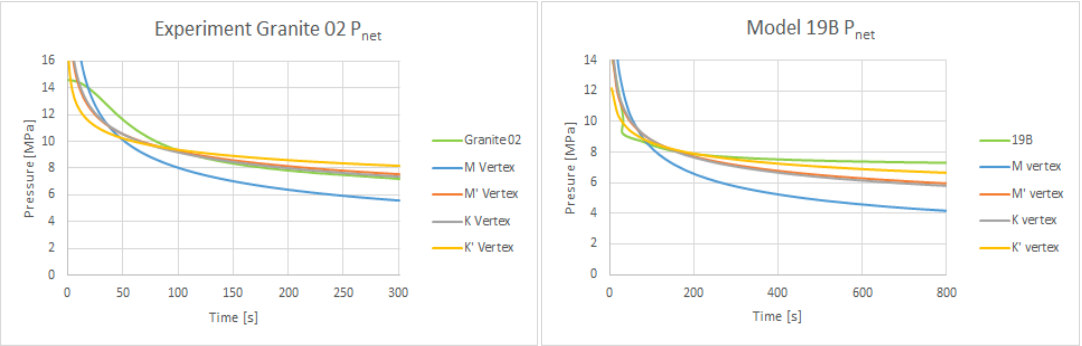


**Figure 2.2.4: P(t) curve of the Granite 02 experiment (left) and the corresponding model 19B (right), until the end of pumping. No good fit for the experiment is obtained due to startup of the experiment. For the model, K' vertex fits best.**

### 2.2.5 Discussion

Our results show that the MFrac™ simulator can definitely be used to scale hydraulic fracturing models, despite the fact that it is oriented towards field simulations. The user interface of the simulator is accessible to scientists without a strong engineering or physics background. Using MFrac™ instead of conducting laboratory experiments can save researchers a lot of time, resources, and possibly finances. Combined with Dontsov's P(t)-curve analysis this makes for a strong tool when the research is oriented towards understanding fracture growth over time.

However, this research and the Mfrac™ simulation tool also has its limitations and weaknesses. The program inherently assumes that the fracture medium is unfractured before treatment. This is highly unlikely in real life. Additionally, the accuracy of the tool is highly dependent on the accuracy of the

inserted parameters. This means that for any sample, a range of properties needs to be measured before MFrac™ can be used to simulate the fracturing experiments. This limits the applicability of the tool.

Lastly, it must be noted that the experiments were conducted using a viscous fluid that will never be used in the field. Half of the models were based on these experiments. The Dontsov analysis shows that only experiment Marble 01 was positively unaffected by the viscosity of the fracturing fluid. As such, GEMex partners looking to apply the current model results must do so with caution.

### 2.2.6 Conclusion

The MFrac™ modelling simulator can be used to scale hydraulic fracturing experiments. However, this is only possible by making several assumptions and scaling some parameters. There must be no fluid leak-off, and it must be assumed that the internal friction is negligible. Scaling the injection rate q linearly with scaling factor S leads to the most accurate model. Additionally, it is crucial to scale the fracture toughness $K_{IC}$ by $S^{\frac{1}{6}}$.

Using Dontsov's approximation of a penny-shaped model to analyze the experiments and corresponding models gave the following results. Two of the three P(t) curves of the model simulations clearly fall in the leak-off toughness regime, also known as the K' vertex. This is surprising, since no leak-off is one of the boundary conditions of the models. The third model matched reasonably well with both the M' and the K vertex: an ambiguous result.

Out of the three experiments, only Marble 01 was positively unaffected by the viscosity of the fracturing fluid (glycerol). This experiment falls in the leak-off toughness regime. Again, this is surprising: the specimen were tested for leak-off as part of the hydraulic experiment. The other two experiments have more ambiguous results: none of the vertex curves fit. This suggests that both viscosity and fracture toughness-related processes affected the fracturing.

The results of the analysis has implications for the in-field applicability of the RWTH laboratory experiments and the models. Hydraulic experiments and models whose fracture propagation has been affected by viscosity-related processes cannot be linearly transcribed to the field, where much less viscous fluids than glycerol are used. Thus GEMex partners are advised to practice caution when using these results.

### 2.2.7 References


1. Baker Hughes. MFracTM suite, n.d.
2. Dekker, E.S.J., 2918. Modelling the GEMex / Aachen marble and granite fracturing experiments in MFracTM. GEMex MSc report.
3. Dontsov, E.V., 2016. An approximate solution for a penny-shaped hydraulic fracture that accounts for fracture toughness, fluid viscosity and leak-off. R. Soc. Open sci. 3
4. Fossen, H., 2010. Structural Geology. New York: Cambridge University Press.
5. Geertsma, J. and de Klerk, F., 1969. A rapid method of predicting width and extent of hydraulically induced fractures. Journal of Petroleum Technology, pages 1571-1581.
6. Geertsma, J. and Haafkens, R., 1979. Comparison of the theories for predicting width and extent of vertical hydraulically induced fractures. Journal of Energy Resource Technology, 101(1):8-19.
7. Gerya T., 2010. Introduction to Numerical Geodynamic Modelling. Cambridge University Press,.
8. Ismail-Zadeh and Tackley, P. 2010. Computational Methods for Geodynamics. Cambridge University Press
9. Lopez-Hernandez et al., 2009, Hydrothermal activity in the Tulancingo–Acoculco Caldera Complex, Central Mexico, Geothermics 38 (2009) 279-293
10. Meyer, B.R. 1986. Design formulae for 2-d and 3-d vertical hydraulic fractures: Model comparison and parametric studies. Paper SPE 15240 presented at the SPE Unconventional Gas Technology Symposium.
11. Meyer, 2011. Meyer Fracturing Simulators User's Guide. Meyer and Associates, inc, 9th edition.
12. Nordgren, R.P. 1972. Propagation of a vertical hydraulic fracture. SPE Journal, pages 306-314.
13. Perkins, T.K. and Kern, L.R. 1961. Width of hydraulic fractures. Journal of Petroleum Technology, pages 937-949.
14. Siebert, Philipp, 2017, Laborversuche zur hydraulischen Risserzeugung in dreiaxial belasteten Granitquadern, Doctoral Dissertation, RWTH Aachen University
15. Valkó, P. and Economides, M.J. 1995. Hydraulic Fracture Mechanics. John Wiley and Sons.
16. Young H.D. and Freedman, R.A. 2012. Sears and Zemansky's University Physics with Modern Physics. Addisson-WesleyPearson Education, Inc., 13th edition.

## 2.3 Institution name: Helmholtz-Zentrum für Umweltforschung – UFZ

*(Francesco Parisio, UFZ Leipzig)*

### 2.3.1 Software used

The software employed for the simulation is OpenGeoSys, a C++ open-source finite element platform for the simulation of three-dimensional thermo-hydro-chemo-mechanical problems in fractured porous media [3]. OpenGeoSys is freely available for download at https://github.com/ufz/ogs and has fully parallelized capabilities with domain decomposition in a three-dimensional framework, several models of inelasticity of porous materials and coupled multi-phase fluid flow in non-isothermal conditions. Versions with couplings with geochemical solvers also exist. The employed model is a lower-dimensional interface elements (LIE) with local enrichment [4] extended to include a cohesive-zone approach based on a bi-linear traction-separation law [5]. The full model implementation and validation against analytical solutions can be found in [5], while here we recall the basic principles and equations.

### 2.3.2 Basic Numerical model

The model contains enrichment at the element boundaries and represents as such a special case of the extended finite element method. The weak form of the static equilibrium equation writes

$$\int_{\Omega\setminus\Gamma_c} \delta\boldsymbol{\varepsilon} : \boldsymbol{\sigma}\, \mathrm{d}\Omega - \int_{\Omega\setminus\Gamma_c} \delta\boldsymbol{u} : \rho\boldsymbol{b}\, \mathrm{d}\Omega - \int_{\partial_N\Omega} \delta\boldsymbol{u}\cdot\bar{\boldsymbol{t}}\, \mathrm{d}\Gamma - \int_{\Gamma_c} \left(\delta\boldsymbol{u}^{+} - \delta\boldsymbol{u}^{-}\right)\cdot\boldsymbol{t}_c\, \mathrm{d}\Gamma = 0\,, \tag{1}$$

where $\boldsymbol{\varepsilon}$ and $\boldsymbol{\sigma}$ are the strain and stress tensors, respectively, $\boldsymbol{u}$ is the displacement vector, $\rho$ is the solid density, $\boldsymbol{b}$ the body acceleration vector, $\bar{\boldsymbol{t}}$ and $\boldsymbol{t}_c$ are surface tractions at the boundary of the model $\partial_N\Omega$ and of the fracture $\Gamma_c$ and the term $\delta\boldsymbol{u}^{+} - \delta\boldsymbol{u}^{-}$ defines the displacement jump across the fracture. The effective stress within the fracture is defined as $\boldsymbol{t}_c = \boldsymbol{t}_c' - p\boldsymbol{n}_\Gamma$, with the pore pressure $p$ and a damage law is proposed to simulate the traction-separation law within the fracture as

$$\boldsymbol{t}_c' = \left[K_n\left(\boldsymbol{n}_\Gamma \otimes \boldsymbol{n}_\Gamma\right) + K_s\left(\boldsymbol{I} - \boldsymbol{n}_\Gamma \otimes \boldsymbol{n}_\Gamma\right)\right]\left(\boldsymbol{u}^{+} - \boldsymbol{u}^{-}\right), \tag{2}$$

where the damage is activated only in tensile mode (i.e., mode I) and degrades compressive stiffness as

$$\boldsymbol{K}^d = \frac{\left(1-d\right)w_{n,p}}{d\left(w_{n,f} - w_{n,p}\right) + w_{n,p}}\boldsymbol{K}\,, \tag{3}$$

where $w_{n,p} = t_{n,p} / K_n$ and $w_{n,f} = 2G_c / t_{n,p}$, $t_{n,p}$ is the normal tensile strength, $K_n$ and $K_s$ are the normal and shear fracture stiffnesses and $G_c$ is the critical energy release rate. Damage increase writes

$$d^{t+\Delta t} = \min\left[1, \max\left(\frac{\left\langle w - w_{n,p}\right\rangle}{w_{n,f} - w_{n,p}}, d^t\right)\right], \tag{4}$$

where $\langle\bullet\rangle$ is the Macauley bracket. The conceptual model, along with the traction-separation law description, is illustrated in Figure 2.3.1.

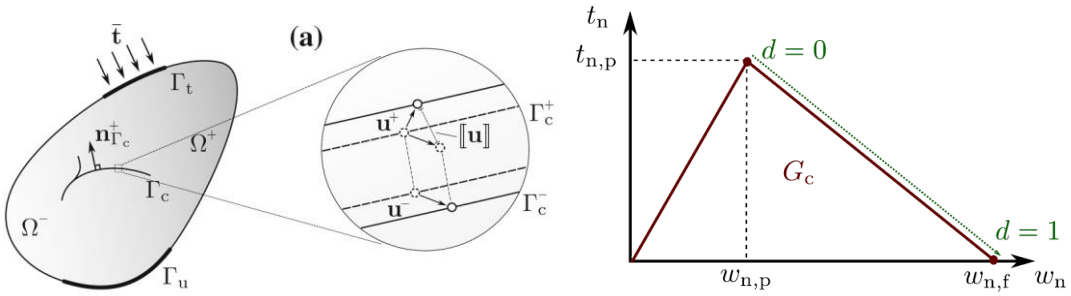


**Figure 2.3.1: Conceptual illustration of a cohesive zone model using lower-dimensional interface elements with local enrichment to represent a strong displacement discontinuity (left) and the traction-separation law employed in this formulation (right) (image from [5]).**

The hydraulic model corresponds to the original implementation of [4], and we report here its essential features. The mass balance within the porous medium writes

$$S_s^m \frac{\partial p^m}{\partial t} + \alpha^m \nabla \cdot \frac{\partial \boldsymbol{u}}{\partial t} + \nabla \cdot \boldsymbol{q} + Q^m = 0\,, \tag{5}$$

where $S_s^m = \left(\alpha^m - n\right)/K^S + n/K^l$ is the storage coefficient of the porous continuum, $p^m$ its pore pressure, $\alpha^m$ is Biot's coefficient, $Q^m$ a source term and the flux $\boldsymbol{q}$ follows Darcy's law

$$\boldsymbol{q} = \frac{\boldsymbol{k}}{\mu}\left(-\nabla p^m + \rho^l \boldsymbol{g}\right), \tag{6}$$

with $\boldsymbol{k}$ the intrinsic permeability tensor, $\mu$ is the fluid dynamic viscosity and $\rho^l$ its density and $\boldsymbol{g}$ is the acceleration of gravity vector. The mass balance within the fracture writes

$$bS_s^f \frac{\partial p^f}{\partial t} + \alpha^f \frac{\partial b}{\partial t} + \nabla \cdot \left(b\boldsymbol{q}\right) + q^+ + q^- = 0\,, \tag{7}$$

where $b$ is the fracture aperture, $S_s^f = 1/K^l$ is the specific storage for the fracture, $\alpha^f$ is Biot's coefficient of the fracture and $q^+$ and $q^-$ the leakage flux from each side of the fracture into the porous medium. Darcy's law for the fracture writes

$$\boldsymbol{q} = \frac{b^2}{12\mu}\boldsymbol{I}\left(-\nabla p^f + \rho^l \boldsymbol{g}\right). \tag{8}$$

### 2.3.3 Numerical model vs analytical solution

Two analytical solutions are employed for comparison against the numerical model. In this case, only the mechanical problem description is employed (no fluid flow) and the pore pressure within the fracture is approximated for the toughness dominated regime following the algorithm reported in [5]. The first solution is relative to an internally pressurized static (non-propagating) crack and the analytical displacement writes [6]

$$u_y^+\left(x,0\right) = \frac{2pa_0\left(1-\nu\right)}{E}\left(1-\frac{x^2}{a_0^2}\right)^{1/2} = -u_y^-\left(x,0\right), \tag{9}$$

where $u_y^+(x,0)$ is the positive vertical opening of the crack (semi-aperture), $p = 10$ MPa is the crack internal pressure, $a_0 = 0.1$m is the crack half-length, $E = 80$ GPa is Young's modulus and $\nu = 0.15$ is Poisson's ratio. The comparison of the static crack displacement is shown in Figure 2.3.2 (left): there is good agreement between the analytical and the numerical (LIE) solutions. The second comparison involves a propagating crack driven by a zero-viscosity fluid. In this case, the pressure is uniform within the fracture, which propagates in the toughness dominated regime [7]. The analytical solution relates pressure within the fracture to the total injected volume as [8]

$$p(V) = \begin{cases} \dfrac{E}{1-\nu}\dfrac{V}{2\pi a_0^2} & \text{if} \quad V \le V_c \\ \left[\dfrac{2EG_c^2}{(1-\nu)\pi V}\right]^{1/3} & \text{if} \quad V > V_c \end{cases}, \tag{10}$$

where the critical volume $V_c = \left(4\pi a_0^3 G_c / E'\right)^{1/2}$ and $E' = E/(1-\nu)$ in plane strain conditions. The critical energy release rate is $G_c = 20$ Pa m. The crack length evolution once the critical volume is reached reads

$$a(V) = \begin{cases} a_0 & \text{if} \quad V \le V_c \\ \left[\dfrac{2EV^2}{4(1-\nu)\pi G_c}\right]^{1/3} & \text{if} \quad V > V_c \end{cases}. \tag{11}$$

The results of this comparison case are illustrated in Figure 2.3.2 (right). The numerical model compares well with the analytical solution both in terms of normalized pressure field and normalized crack length. Figure 2.3.3 compares stress profiles at different locations across the crack. The model well reproduces the stress field and the zero-stress transfer at the crack faces (Figure 2.3.3a), along with the crack-tip singularity (Figure 2.3.3b and Figure 2.3.3c) consistent with the theory of linear elastic fracture mechanics. Additional details about calculations and the algorithm employed to fluid drive crack propagation in the toughness dominated regime are reported in [5].

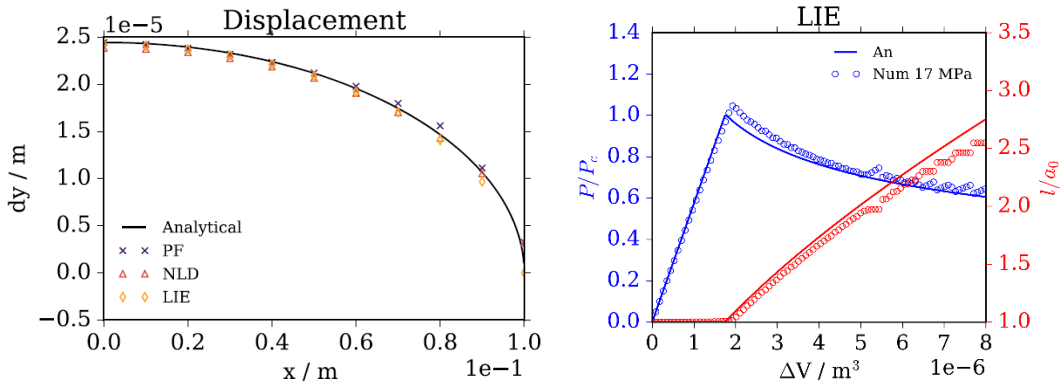


**Figure 2.3.2: Analytical vs numerical solution of a static pressurized crack (left) and of normalized pressure and crack length evolution during fluid driven crack propagation example (right, image from [5]).**

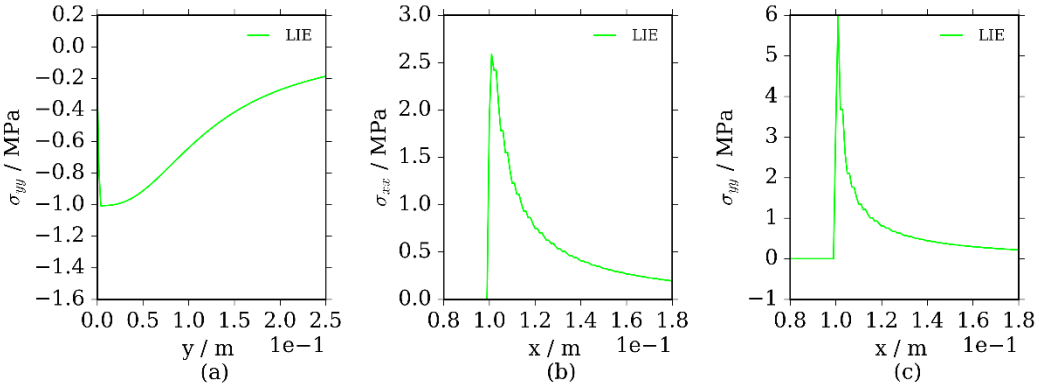


**Figure 2.3.3: Stress profiles for the numerical model: vertical stress along a central vertical line (a), horizontal stress along a central horizontal line (b) and vertical stress along a central horizontal line (c) (image from [5]).**

### 2.3.4 Numerical model vs experimental data set

The experimental data set employed for the comparison (VV34) was described in a previous report [2] and is in all aspects similar to the experiments described in this report, with slightly different values of the material parameters. In this case, the full hydro-mechanical problem is solved, taking into account fluid flow within the fracture and viscous dissipation forces. This is because glycerol is used as a fluid, which has a higher viscosity than water: hence, the hypothesis of toughness-dominated regime is not valid anymore and viscous dissipation forces need to be taken into account. This is achieved with the full hydro-mechanically couple LIE model. To study further the problem, we also employ an analytical solution of fluid-driven crack propagation [9]. The fluid is glycerol with density $\rho^f = 1000\,\text{kg/m}^3$ and dynamic viscosity $\mu = 1.5\,\text{Pa s}$, the porous medium has density $\rho^s = 2680\,\text{kg/m}^3$, porosity $n = 0.02$, intrinsic permeability $\boldsymbol{k} = 1\times10^{-19}\,\boldsymbol{I}\ \text{m}^{-2}$, storage coefficient $S_s^m = 1.3\times10^{-10}\,\text{Pa}^{-1}$, Biot's coefficient $\alpha^m = 0.5$, Young's modulus $E = 36.9\,\text{GPa}$ and Poisson's ratio $\nu = 0.3$. The fracture has a storage coefficient of $S_s^f = 6.9\times10^{-9}\ \text{Pa}^{-1}$, Biot's coefficient $\alpha^f = 1$, normal and shear stiffness $K_n = K_s = 1\times10^{20}\,\text{Pa}$ in order to simulate full stress transfer (equivalent to intact rock), critical energy release rate $G_c = 75\,\text{Pa m}$, tensile strength $t_{n,p} = 75\,\text{MPa}$ and the injection rate is $q_{in} = 8.33\times10^{-10}\ \text{m}^3/\text{s}$. The high value of tensile strength is set in order to achieve high brittleness of the response, since the global strength is instead determined by the energy release rate and the tensile strength can be employed to control rate of softening. Special attention is dedicated to the computation of the storage coefficient in the fracture, which is the inverse of the fluid compressibility $S_s^f = 1/K^l$: because the pressure is monitored upstream, the whole system compressibility is computed as

$$\frac{1}{K^{system}} = \frac{V_{system}}{V_{notch}}\frac{1}{K^l}, \tag{12}$$

where $V_{system} = V_{pump} + V_{pipe} + V_{notch}$ is the whole system volume (pipe + pump + notch), $V_{notch}$ is the volume of the initial fracture (notch) and $1/K^{system}$ is the whole system compressibility. The whole system volume is $V_{system} = 1.38\times10^{-5}\ \text{m}^3$ and the volume of the notch is $V_{notch} = 3.56\times10^{-7}\ \text{m}^3$, which, for a fluid compressibility of $1/K^l = 2.10\times10^{-10}\,\text{Pa}^{-1}$ gives a system compressibility

$1/K^{system} = 8.15\times10^{-9}$ Pa$^{-1}$. This value is further fitted to better represent the experimental values to $1/K^{system} = S_s^f = 6.9\times10^{-9}$ Pa$^{-1}$. Because of symmetry conditions, the numerical model is axisymmetric around the well axis and horizontal and vertical stresses are applied as boundary conditions. The flow is injected in the initial notch.

The analytical solution follows the algorithm proposed by [10] and we have employed the script provided in the original publication for the simulations. The analytical solution is based on the theory of fluid driven crack-propagation in porous media, which considers a penny-shaped fracture that propagates radially and quasi-statically in a permeable, linear elastic medium and is driven by a pressurized incompressible Newtonian fluid [9]. The governing equations of the analytical solution are the continuity equation within the fracture

$$\frac{\partial b}{\partial t}+\frac{1}{r}\frac{\partial}{\partial r}(rq)+\frac{2C_L}{\sqrt{t-t_0(r)}}=Q_0\delta(r)\ , \tag{13}$$

where $q$ is the fluid flow in the radial direction, $C_L$ is a leak-off coefficient, $t_0(r)$ is the time in which the fracture front is located at radial coordinate $r$ and $Q_0$ is the constant injection rate within the fracture origin (pointwise injection). The equation of linear elastic equilibrium writes

$$p(r,t)=-\frac{E'}{R}\int_0^1 \mathrm{X}(\rho,s)\frac{\partial b}{\partial s}\mathrm{d}s\,, \tag{14}$$

where $p(r,t)$ is the fluid pressure in the fracture, $\rho = r/R$ is the radius-normalized coordinate and the kernel function $\mathrm{X}$ is

$$\mathrm{X}(\rho,s)=\frac{1}{2\pi}\begin{cases}\dfrac{1}{\rho}\Lambda\left(\dfrac{s^2}{\rho^2}\right)+\dfrac{\rho}{s^2-\rho^2}\Xi\left(\dfrac{s^2}{\rho^2}\right) & \rho>s\\ \dfrac{s}{s^2-\rho^2}\Xi\left(\dfrac{s^2}{\rho^2}\right) & \rho\le s\end{cases}, \tag{15}$$

with $\Lambda(\bullet)$ and $\Xi(\bullet)$ complete elliptic integrals of the first and second kind, respectively. The flow in the fracture follows Poiseuille's equation

$$q=-\frac{b^3}{12\mu}\frac{\partial p}{\partial r}\,, \tag{16}$$

and the fluid balance equation (injected volume = volume in the crack + volume leaked off) is

$$\frac{1}{2\pi}\int_0^t Q_0\mathrm{d}t=\int_0^R rb\,\mathrm{d}r+\int_0^t\int_0^{R(\tau)} r\frac{2C_L}{\sqrt{t-t_0(r)}}\mathrm{d}r\,\mathrm{d}\tau\,. \tag{17}$$

The fracturing of the porous media is governed by linear elastic fracture mechanics behaviour and the propagation criterion writes

$$K_I = \frac{2}{\sqrt{\pi R}} \int_0^R \frac{p(r,t)}{\sqrt{R^2 - r^2}} r \, \mathrm{d}r \,, \tag{18}$$

with $K_I$ being the stress intensity factor in Mode I, which, based on the no-lag assumption (fluid front and crack tip coincide), is also the material toughness $K_{Ic}$. The opening at crack tip writes

$$w \approx \frac{8}{\sqrt{2\pi}} \frac{K_I}{E'} \sqrt{R - r}, \quad 1 - \frac{r}{R} \approx 1 \tag{19}$$

and the crack propagates unstably when $K_I = K_{Ic}$. The solution of this problem was widely explored in the literature (cf. [7] for a detailed and complete review on the subject) and four primary asymptotic regimes of propagation have been identified, in which one of the two dissipative mechanism and one of the two fluid storage components vanishes: i) storage viscosity $M$, ii) storage toughness $K$, iii) leak-off viscosity $\tilde{M}$, and iv) leak-off toughness $\tilde{K}$. $M$ and $\tilde{M}$ solutions have negligible toughness, $K$ and $\tilde{K}$ solutions have negligible viscosity. In $\tilde{M}$ and $\tilde{K}$ solutions the fluid leaks-off into the formation and in $M$ and $K$ solutions the fluid is stored in the fracture. The full solution for the four vertices and for the intermediate cases are reported in literature [7, 10]. We have computed the evolution of pressure with time for the toughness-storage and the viscous-storage regimes. We have neglected leak-off because of the low permeability of the granite and the high viscosity of the fluid, which globally concur to reduce the leak-off. The results of the numerical and analytical calculation and the comparison against the experimental values are illustrated in Figure 2.3.4 and Figure 2.3.5.

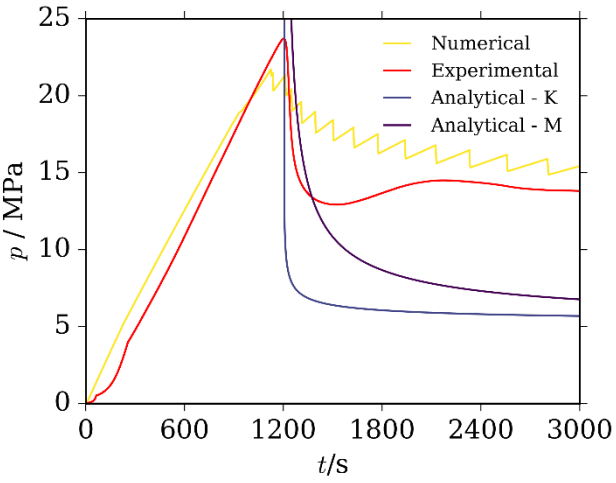


**Figure 2.3.4: Analytical and numerical solutions of pressure curve compared against experimental findings.**

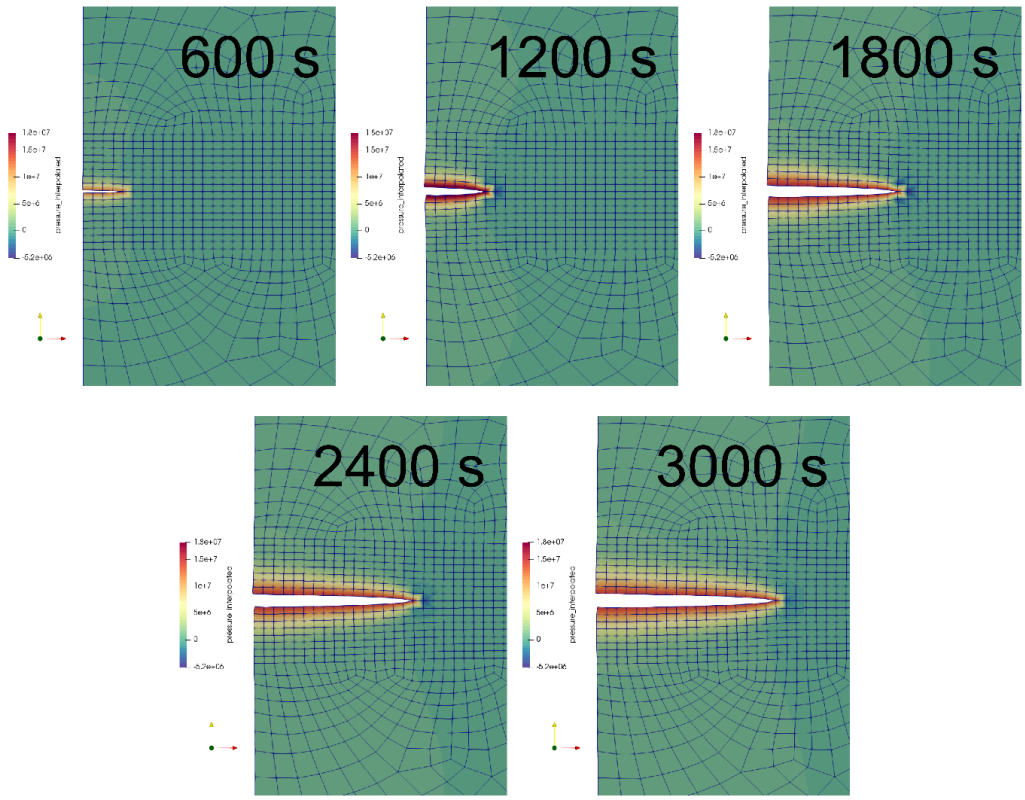


**Figure 2.3.5: Crack aperture (100 times magnified) and pore pressure field evolution from the numerical analysis.**

### 2.3.5 Discussion

The numerical method employed (hydro-mechanical lower interface elements coupled with cohesive-zone model approach) can successfully simulate fluid-driven fracture propagation in the toughness dominated regime and compares well with the analytical solutions. The crack aperture in the static case is correctly computed and the pressure and crack length vs volume responses are also correct. The stress transfer is also properly reproduced and globally, the method is sound in predicting both the dynamic and kinematics of fluid driven fracture propagation.

Both analytical solutions in the toughness and in the viscous regimes are asymptotic toward the external state of stress, as the no-lag hypothesis implies that the stress field does not influence the crack propagation. Instead the experiment shows an asymptote in the pressure curve which is higher than the vertical state of stress applied (5 MPa), a hint toward possible boundary effects. The viscous vertex solution performs better than the toughness one, which points to the fact, which is important to take into proper account viscosity effects in this specific case. Both analytical solutions fail to deliver proper results, as, despite the significant size of the model, boundary effects are still pronounced.

The numerical solution oscillates and exhibits chainsaw type of curve, which is a combination of the high brittleness and the mesh resolution employed. Once an element undergoes failure, the stress drops instantaneously and the additional stress is transferred to the element ahead of the crack tip. The pressure increases until an additional element fails, and the cycle is repeated. Despite this, the numerical model exhibits an asymptotic behaviour which is in fairly good agreement with the experimental results. The breakout pressure is slightly underestimated, and the strong pressure drop observed in the experiment is not properly reproduced by the numerical model, which instead shows a much weaker softening rate in the early stages of breakout.

During fracture propagation, pressure diffuses in the rock matrix in the vicinity of the crack faces. The areas affected by pressure increment are larger with time as the fluid slowly diffuses into the porous medium. Though model can correctly reproduce the fracture propagation coupled with fluid flow, some shortcomings are still present.

### 2.3.6 Conclusion

We have presented a numerical method to simulate the propagation of fluid-driven fractures in porous media that takes into account displacement discontinuity, viscous flow in the fracture and leak-off from fracture to matrix. The model was previously developed to simulate existing fractures and has been further extended to take into account the propagation of newly created fractures. Because the lower-interface element method accounts for enhanced kinematic description at the element boundaries, the fracture trajectory cannot rotate during propagation and the mesh must be conforming to the fracture geometry. For pure mode I propagation, the trajectory is known a-priori and this does not pose further limitations. Extensions are required to simulate mixed mode propagation and curved fracture trajectories. Such extensions could be h-adaptive re-meshing algorithms and element orientation corrected fracture criteria. The model proved to be correct in predicting propagation in the toughness dominated regime and compares well with the analytical solution in terms of fracture dynamics and kinematics. The fracture aperture, the pressure response and the crack growth are in agreement with analytical solutions. The analytical solutions fail to deliver proper predictions when compared against the experiments because of the boundary effect. The asymptotes are not in agreement and the analytical solutions tend to the external vertical stress applied. The numerical model performs better in terms of global response and simulates correctly the experimental response in terms of elastic response, pressure breakout and the asymptotic pressure decay at large injected volume. The oscillating behaviour is a consequence of the adopted mesh size and further developments, such as adaptive re-meshing and parallelized calculations to reduce computational time would improve the performances, allowing running simulation with smaller meshes that could remove the saw-tooth pressure oscillations.

### 2.3.7 References


1. Lopez-Hernandez et al., 2009, Hydrothermal activity in the Tulancingo–Acoculco Caldera Complex, Central Mexico, Geothermics 38 (2009) 279-293.
2. Siebert, Philipp, 2017, Laborversuche zur hydraulischen Risserzeugung in dreiaxial belasteten Granitquadern, Doctoral Dissertation, RWTH Aachen University.
3. Kolditz et al., 2012, OpenGeoSys: an open-source initiative for numerical simulation of thermo-hydro-mechanical/chemical (THM/C) processes in porous media, Environmental Earth Sciences 67.2: 589-599.
4. Watanabe et al., 2012, Lower-dimensional interface elements with local enrichment: application to coupled hydro-mechanical problems in discretely fractured porous media, International Journal for Numerical Methods in Engineering 90.8: 1010-1034.
5. Yoshioka et al., 2019, Comparative verification of discrete and smeared numerical approaches for the simulation of hydraulic fracturing, GEM-International Journal on Geomathematics 10.1: 13.
6. Ji et al., 2009, A novel hydraulic fracturing model fully coupled with geomechanics and reservoir simulation, SPE Journal 14.03: 423-430.
7. Detournay, 2016, Mechanics of hydraulic fractures, Annual Review of Fluid Mechanics 48: 311-339.
8. Sneddon et al., 1969, Crack problems in the classical theory of elasticity, 221 P.
9. Savitski et al., 2002, Propagation of a penny-shaped fluid-driven fracture in an impermeable rock: asymptotic solutions, International Journal of Solids and Structures 39.26: 6311-6337.
10. Dontsov, 2016, An approximate solution for a penny-shaped hydraulic fracture that accounts for fracture toughness, fluid viscosity and leak-off, Royal Society open science 3.12: 160737.


Coordination Office, GEMex project

Helmholtz-Zentrum Potsdam
Deutsches GeoForschungsZentrum

Telegrafenberg, 14473 Potsdam

Germany